RSC Advances

ROYAL SOCIETY OF CHEMISTRY

PAPER

View Article Online
View Journal | View Issue

Cite this: *RSC Adv.*, 2025, **15**, 47545

Acid-phase protection of low-carbon steel by DIMC: evidenced by WL/PDP/EIS and density-functional modeling

Sherin A. M. Ali,[a] Mostafa E. Salem,[b] Mostafa A. A. Mahmoud,[*cd] Mansour Alsarrani,[e] Mohamed Abdel-Megid,[b] H. A. El Nagy[c] and Ahmed Z. Ibrahim[cf]

Received 11th October 2025
Accepted 26th November 2025

DOI: 10.1039/d5ra07780j

rsc.li/rsc-advances

We synthesized and evaluated 2,2′-(2,3-dihydroxyterephthaloyl)bis(*N*-propylhydrazine-1-carbothioamide) (DIMC) as a corrosion inhibitor for low-carbon steel (LCS) in 0.5 M HCl. A multi-technique workflow—weight loss (WL), potentiodynamic polarization (PDP), electrochemical impedance spectroscopy (EIS), and surface analysis (SEM/AFM)—shows concentration-dependent protection with maximum inhibition efficiency of 91.41% at 300 ppm and 298 K, remaining 80.24% at 328 K. EIS reveals two distinct time constants; refitting with R_s–(C_{dl}‖R_{ct})–(Cfilm‖Rfilm) confirms robust charge-transfer suppression plus a film-relaxation response. DFT descriptors and Monte Carlo adsorption simulations corroborate mixed physisorption–chemisorption, with electron-rich N/S/O centers driving donor–acceptor interactions at Fe sites. Collectively, DIMC forms a stable adsorbed layer that mitigates both anodic and cathodic reactions in aggressive acid, positioning DIMC as a promising green inhibitor for acid-exposed steel systems.

1 Introduction

Corrosion—the progressive deterioration of a material through interaction with its surrounding environment—remains an inherent and continual hazard in oil and gas production and transportation, where equipment is routinely exposed to complex fluids and dynamic operating conditions.[3–6] In this context, carbon steel (C-steel) tubing is widely favored for gathering, production, and flow-line service because it combines low cost with ease of fabrication and reliable mechanical performance. Despite these advantages, C-steel is vulnerable to pronounced attack in aggressive media, most notably formation water, which is consistently identified as one of the harshest and most consequential environments encountered in oilfield processes.[7–9] Compounding the challenge, crude oil and natural gas often carry corrosive impurities, and the downhole and pipeline environments frequently contain highly reactive species such as carbon dioxide (CO_2), hydrogen sulfide (H_2S), and free water that accelerate metal dissolution and undermine long-term asset integrity.[10]

Under such conditions, organic, synthetically accessible corrosion inhibitors—including members of the DIMC family—are particularly attractive when they are designed from low-toxicity building blocks, degrade more benignly, and avoid ecotoxic residues; resorcinol-based motifs are a compelling platform in this regard.[2] The continuous coproduction and transport of CO_2, H_2S, and water across long residence times further aggravate internal attack on tubing, flowlines, and surface equipment.[11] Among these drivers, CO_2-induced corrosion has received sustained attention, both because CO_2 is naturally present in many reservoirs and because it is intentionally injected during enhanced-oil-recovery operations; once dissolved, CO_2 forms carbonic acid which accelerates both uniform corrosion and localized phenomena on steel surfaces.[12–16] In practice, corrosion inhibitorstherefore remain one of the most practical and cost-effective levers for mitigating damage, extending service life, and preserving structural integrity across upstream and midstream infrastructure.[17]

Although the present study employs 0.5 M HCl as the experimental electrolyte, this medium is widely recognized as a bench-scale surrogate that captures the essential chemistry of acid stimulation used in oil production. In such operations,

[a]*Department of Mechanics, Faculty of Engineering, Suez Canal University, Ismailia 41522, Egypt*

[b]*Chemistry Department, College of Science, Imam Mohammad Ibn Saud Islamic University (IMSIU), Riyadh 11623, Saudi Arabia. E-mail: meaSalem@imamu.edu; moabmohamed@imamu.edu.sa*

[c]*Department of Chemistry, Faculty of Science, Suez Canal University, Ismailia 41522, Egypt*

[d]*Egyptian Company for Natural Gases (GASCO), Ministry of Petroleum, Cairo, Egypt. E-mail: maam403.ms@gmail.com; Tel: +201063644726*

[e]*Department of Chemistry, Faculty of Science, Al-Baha University, Alaqiq, Saudi Arabia. E-mail: malsarrani@bu.edu.sa*

[f]*General Petroleum Company, Research and Development Department, Cairo, Egypt. E-mail: a.zaki_89@yahoo.com*

mineral acids intensify steel dissolution, and the synergistic effects of protons, chloride ions, and occasionally CO_2/H_2S often amplify the severity of attack; hence, evaluating inhibitor response in HCl is an industrially meaningful proxy for screening protection strategies and comparing formulations under controlled conditions. At the same time, the oil and gas sector continues to face a gap between performance and safety/benignity: numerous highly efficient inhibitors are also hazardous, underscoring the need to design environmentally considerate alternatives without sacrificing protection.[18] Fundamentally, inhibitor performance reflects the creation of a protective, adsorbed barrier at the metal/solution interface. Adsorption may proceed *via* physisorption, dominated by electrostatic attraction between charged surfaces and ionic/protonated inhibitor species, and/or *via* chemisorption, where donor–acceptor interactions and coordination-type bonding anchor the inhibitor to surface sites.[19–22]

Against this backdrop, we synthesized a new set of dihydroxy-isophthalohydrazine-derived inhibitors from low-cost resorcinol derivatives and ethyl isothiocyanate, and evaluated their ability to protect C1018 steel using a complementary electrochemical toolset.[23,24] To contextualize interfacial changes, the surface morphology of treated and untreated specimens was characterized by SE and AF microscopy, while trends in inhibition efficiency were correlated with theoretical calculations, consistent with extensive literature that links molecular electronic structure to adsorption and macroscopic protection. For instance, Ankush Mishra *et al.* reported that 5-amino pyrazole carbonitriles (AHPC) achieved 90.34% inhibition on mild steel in 1 M HCl, with electrochemical evidence of mixed-type behavior and an increased charge-transfer resistance.[25] Similarly, Ashraf M. Ashmawy and co-workers examined a pyrazolone–sulfonamide hybrid (6a) in 1 M HCl, reaching 94.02% efficiency.[26] Waleed M. Saad *et al.* identified 50 ppm as an optimal dose for CIN, delivering 89.68% inhibition.[27] In a complementary weight-loss study, Iman Adnan Annon *et al.* assessed an MPO inhibitor across 1–48 h and 0.1–1.0 mM; at 0.5 mM, the inhibitor achieved 87.6% (303 K) to 92.9% (333 K) over 5 h, highlighting the sensitivity of protection to dosage and temperature.[28]

Building on these advances, the current work introduces 2,2′-(2,3-dihydroxyterephthaloyl)bis(*N*-propylhydrazine-1-carbothioamide) (DIMC) as a candidate mixed-mode inhibitor engineered to present multiple adsorption-active groups (–OH, –NH, –C═S) capable of engaging steel through complementary physisorption and chemisorption pathways (Scheme 1). The molecular scaffold draws deliberately on prior successes with resorcinol-based inhibitors and on the known film-forming propensity of hydrazine/thiourea-type functionalities, which together promote persistent interfacial coverage and barrier formation under acidic conditions.[29] Benchmarking against structurally related analogues underscores the advantage of DIMC: based on EIS measurements at 300 ppm, the inhibition efficiencies of DIMC, DIH, and DDIP are 91.70%, 86.20%, and 82.40%, respectively—evidence of the superior mitigation delivered by the present derivative. In a broader context, comparison with representative organic inhibitors further affirms the effectiveness of DIMC under the conditions studied (see Table 1).[30]

Table 1 Show the IE% of DIMC in contrast with other organic compounds

Inhibitors	Sample	Medium	IE%	References
DDIP	LCS	0.5 M HCl	82.40	1
DIH	LCS	0.5 M HCl	86.20	2
DMIH	MS	0.5 M HCl	88.80	17
6a	MS	0.5 M HCl	94.02	18
CIN	MS	1.0 M HCl	89.68	19
MPO	MS	1.0 M HCl	92.90	20
DIMC	LCS	1.0 M HCl	91.50	Our work

Although 15 wt% HCl is frequently used during field acidizing, 0.5 M HCl remains a rigorous bench-scale proxy that enables controlled electrochemical/gravimetric/theoretical correlation and comparability across the literature. We therefore deploy 0.5 M HCl for mechanism-focused evaluation, while noting that engineering translation will require concentration scaling and validation at field-realistic acid strengths.

2 Experimental

2.1 Materials and solutions

Low-carbon steel (LCS) coupons were sourced from Metal Samples Company with the following composition (wt%): C 0.20, Mn 0.60, Si 0.03, P 0.04, and the balance Fe. Specimens for EIS and potentiodynamic polarization (PP) were cut to 1.0 × 1.0 cm. Prior to use, each coupon was sequentially ground with 400, 600, and 1000-grit emery papers, thoroughly rinsed with double-distilled water, degreased with ethanol, and air-dried at room temperature. Prepared coupons were then immersed in the test solution for 24 h before measurements.

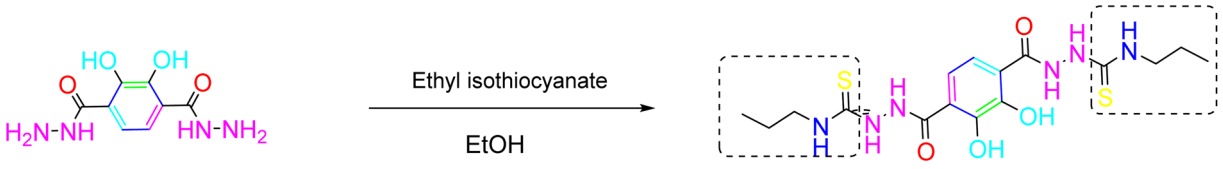

Scheme 1 Synthesis of DIMC by reacting 2,3-dihydroxyterephthaloyl dihydrazide with n-propyl isothiocyanate in ethanol (reflux, 9 h). The product is filtered hot, washed with cold EtOH, and recrystallized from EtOH to afford DIMC (pale solid; high yield). Structure confirmed by ^{1}H/^{13}C NMR (DMSO-d_6) and HRMS.

All chemicals were of analytical grade and obtained from Sigma-Aldrich, including high-quality resorcinol derivatives, ethyl isothiocyanate, hydrochloric acid (37% w/w), acetone, ethanol, and methanol. The corrosive electrolyte was 0.5 mol L^{-1} HCl, freshly prepared for each experiment by diluting concentrated HCl (37% w/w) with double-distilled water to minimize contamination and ensure consistency.

Electrochemical tests were performed on a Bio-Logic instrument using a three-electrode configuration: platinum as the counter electrode, a saturated calomel electrode (SCE) as the reference, and the LCS coupon as the working electrode.

2.2 Synthesis of DIMC chemical

Synthesis of 2,2′-(2,3-dihydroxyterephthaloyl)bis(*N*-propylhydrazine-1-carbothioamide) (DIMC).

2,3-Dihydroxyterephthaloyl dihydrazide (10 mmol) was dissolved in ethanol (30 mL). *n*-Propyl isothiocyanate (10 mmol) was added dropwise under stirring, and the mixture was refluxed for 9 h (TLC monitoring). After cooling, the precipitate was filtered, washed with cold ethanol, and recrystallized (EtOH) to give DIMC (typical yield ≥85%; m.p. > 300 °C).

2.3 Wt. loss method

Weight-loss (WL) experiments were performed in accordance with ASTM G1-29 standard practice. Polished carbon-steel specimens measuring 2.0 cm × 2.0 cm × 0.10 cm were fully immersed in 100 mL of 0.5 mol per L HCl. Each exposure ran for 24 h and was conducted at controlled temperatures spanning 25 °C to 55 °C (298–328 K). To quantify the influence of the synthesized inhibitor, parallel trials were executed in the absence and in the presence of the molecule at concentrations ranging from 50 ppm to 300 ppm.

At the end of the exposure period, the steel coupons were retrieved, air-dried, carefully cleaned, and weighed to determine mass loss. To ensure reproducibility and statistical robustness, every test condition was performed in triplicate. The WL results are reported as the mean value accompanied by the standard deviation (SD) for each condition.

2.4 Electrochemical testing

Electrochemical tests—namely potentiodynamic polarization (PDP) and electrochemical impedance spectroscopy (EIS)—were carried out in a conventional three-electrode glass cell comprising a saturated calomel electrode (SCE) as the reference, a platinum counter electrode, and low-carbon steel (LCS) as the working electrode. Before each run, the LCS working electrode was immersed in the electrolyte until a stable open-circuit potential (OCP) was attained. Measurements were acquired using a Bio-Logic SP-150 potentiostat, with control and data logging *via* EC-LAB software at 298 K.

For PDP (Tafel) experiments, the electrode potential was swept automatically at a scan rate of 0.5 mV s^{-1} from −1400 mV to +300 mV relative to OCP; unless otherwise stated, all potentials are reported *vs.* SCE. Tafel extrapolation was applied to determine the electrochemical corrosion parameters: the corrosion current density (i_{corr}) was obtained by extrapolating the linear regions of the cathodic and anodic branches of the polarization curves back to the corrosion potential (E_{corr}).

For EIS, spectra were recorded at OCP using a small-signal sinusoidal perturbation of 5 mV (peak-to-peak) over a frequency window of 100 kHz to 50 Hz. The resulting impedance responses are presented in both Nyquist and Bode formats. Data acquisition was performed on a personal computer, while plotting and curve fitting were completed using Origin 2018 in conjunction with Microsoft Office 2016 for figure preparation and tabulation. To verify repeatability, each electrochemical condition was tested in triplicate, and the reported values reflect the aggregated results for those replicates.

2.5 Surface analysis study

Low-carbon steel (LCS) specimens were mechanically polished using abrasive papers spanning grit 400 to 1100. After polishing, samples were thoroughly rinsed with deionized water and then immersed in 0.5 mol per L HCl for 48 h to evaluate and purge any potential organic residues. Subsequently, the specimens were rinsed again with deionized water, dried, and subjected to analysis without further treatment. Surface imaging was performed using scanning electron microscopy (SEM, JEOL JSM-6510 LV) and atomic force microscopy (AFM, Keysight 5600LS large-stage system, USA).

2.6 Calculations using quantum chemistry

Quantum-chemical descriptors were obtained by DFT (Opt + Freq) at the B3LYP/6-31+G(d′,p′) level using Gaussian 09, and the resulting structures and orbitals were visualized in GaussView 6.0. Monte Carlo adsorption simulations were performed with a force-field-based geometry optimization workflow using the Adsorption Locator on an Fe(110) surface, employing simulated annealing with the ultrafine setting.

3 Results and discussion

3.1 Analyzing and interpreting DIMC compound confirmation data

Fig. 1 shows the ^{1}H-NMR and ^{13}C-NMR confirmation chart of the synthesized DIMC compound where the peaks are interpreted as the following,

^{1}H-NMR (DMSO-d_6, 400 MHz): δ ∼0.85 (t, 6H, 2 × CH_3, *n*-Pr), 1.45–1.70 (m, 4H, 2 × CH_2, *n*-Pr), ∼3.00 (t, 4H, 2 × NCH_2), 6.8–7.7 (m, ∼2H, aromatic), 9.2–9.5 (br s, 2H, NH), 10.8–11.8 (br s, 2H, phenolic OH), 11.2–12.8 (br s, 2H, thioamide NH).

^{13}C-NMR (DMSO-d_6, 100 MHz): δ ∼14–15 (CH_3), 22–26 (CH_2), ∼40–50 (NCH_2), 116–137 (Ar–C), 150–169 (C–O/C=N), ∼182–190 (C=S). Elemental analysis calculated for $C_{16}H_{24}N_6O_4S_2$ (428.5): C, 44.85; H, 5.65; N, 19.61 found: C, 44.88; H, 5.71; N, 19.64.

3.2 Wt. loss measurements

3.2.1 Effect of DIMC concentration. Under oxygenated acidic chloride media, LCS corrosion involves: Fe → Fe^{2+} + 2e^-; Fe^{2+} + 2Cl^- ⇌ $FeCl_2$(aq); and O_2 + 4H^+ + 4e^- → 2H_2O. Chloride anions destabilize incipient passive films and promote localized

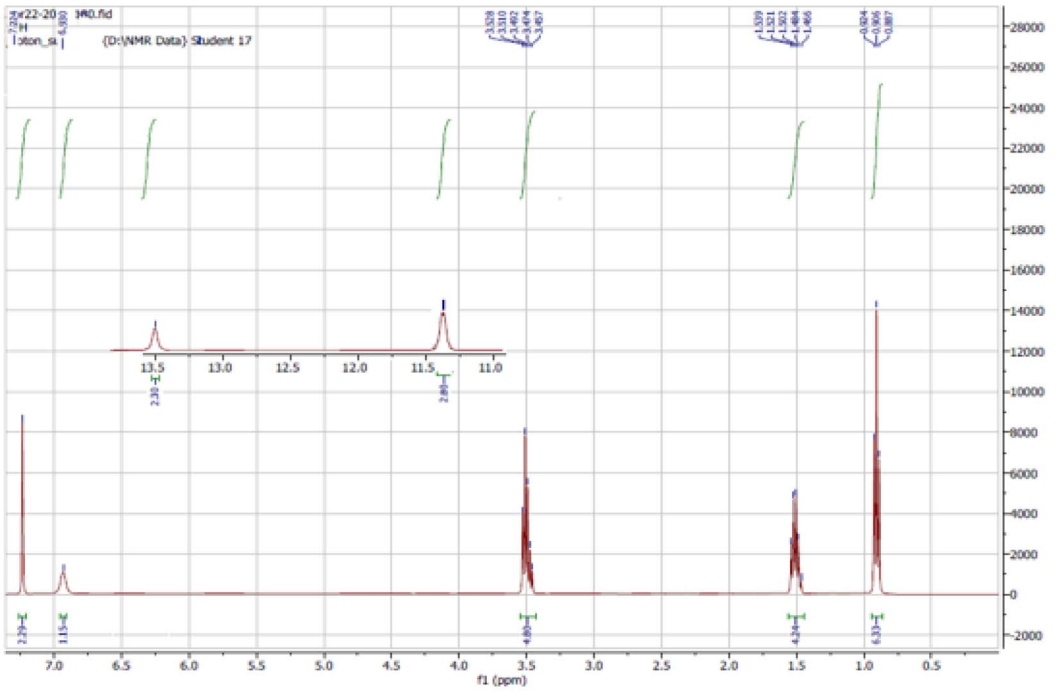

A

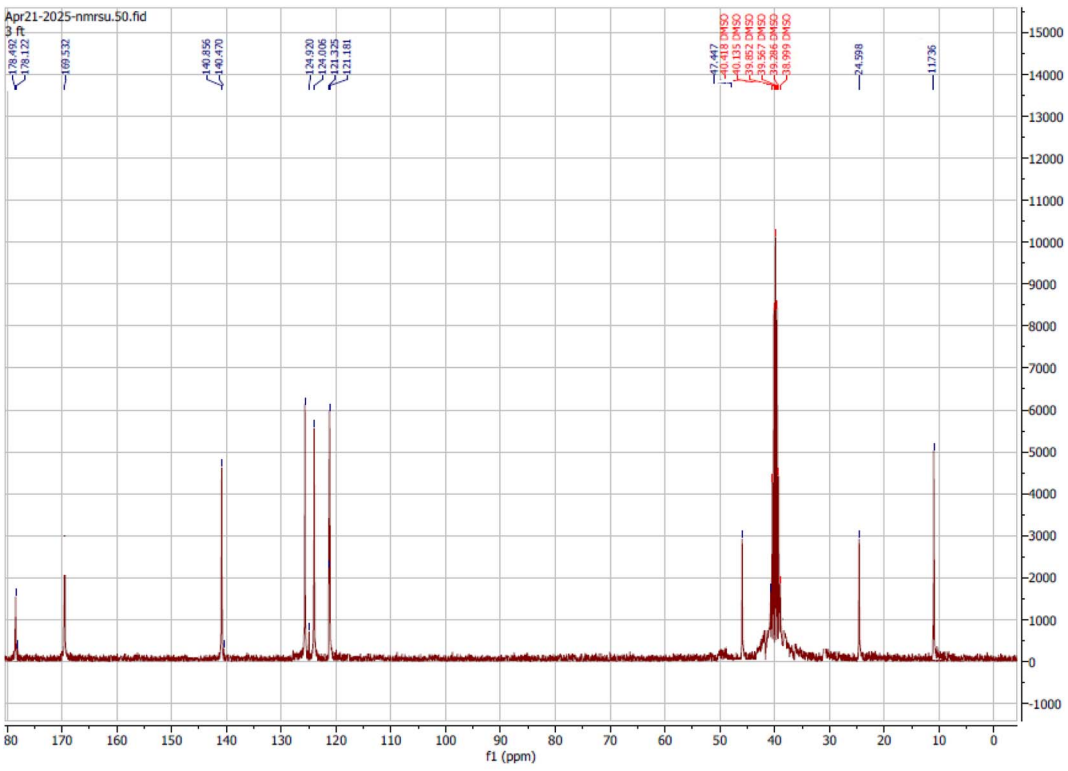

B

Fig. 1 (A) ^{1}HNMR of DIMC synthesized compound in DMSO-d_6, (B) ^{13}CNMR of DIMC synthesized compound recorded in DMSO-d_6.

attack by adsorbing at defect sites, increasing pitting susceptibility.

Compared with other evaluation techniques, the weight-loss (WL) method provides a direct, highly quantitative measure of an inhibitor's effectiveness, yielding corrosion metrics that remain representative of practical service conditions. Accordingly, WL of low-carbon steel (LCS) in 0.5 mol per L HCl was assessed as a function of immersion time, both in the absence

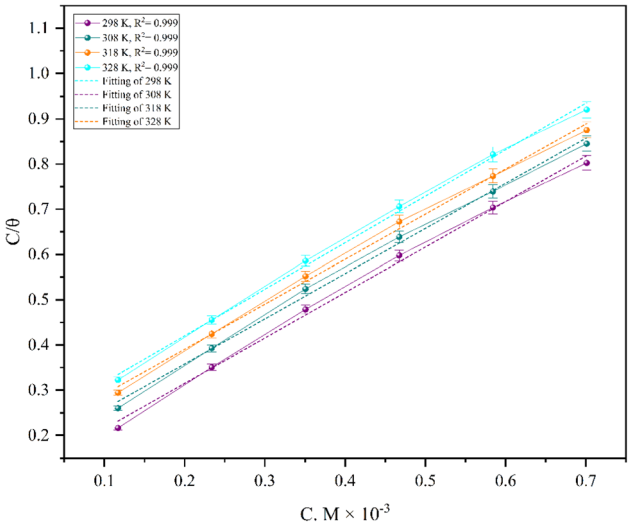

Fig. 2 Langmuir adsorption isotherm for the compound DIMC on LCS in 0.5 mol per L HCl at different temperatures.

and presence of DIMC over the concentration range 50–300 ppm, at temperatures spanning 298–328 K. Based on the surface-coverage values obtained from WL data, Fig. 2 presents the Langmuir adsorption isotherm for DIMC on LCS at 298 K (plotted as C/θ *vs.* C). The linear trend depicted in the figure captures how the system's response evolves with inhibitor dosage; the slope of the line reflects the variation in the corrosion rate of LCS with DIMC concentration as determined from mass loss per unit time. The corrosion rate (k), the weight-loss-based inhibition efficiency (IEw), and the surface coverage (θ) were computed for both the blank electrolyte and the DIMC-containing solutions using eqn (1) and (2).

$$K = \frac{\Delta W}{At} \quad (1)$$

where ΔW represents the mass loss of the LCS coupon (in kilograms), A denotes the exposed surface area of the coupon (in square meters), and t is the immersion time (in seconds).

$$IE_w = 1 - W_{inh}/(W_{corr}) \quad (2)$$

Table 3 Data of WL measurements for carbon steel in 0.5 mol per L HCl solution in the absence and presence of different concentrations of the investigated compound at 298 K. The immersion time is 360 minutes

DIMC			
C (ppm)	$K \times 10^{-3}$ mg cm^{-2} min^{-1}	θ	IE%
Blank	128.0	—	—
50	54.00	0.58	57.81
100	46.00	0.64	64.06
150	36.00	0.72	71.88
200	27.50	0.79	78.51
250	19.20	0.85	85.00
300	10.94	0.92	91.48

W_{corr} and W_{inh} represent the WL of the LCS coupons without and with the inhibitor, respectively. Table 2 displays the WL data for LCS after 360 minutes of immersion in 0.5 mol per L HCl, with and without the synthesized inhibitor at different temperatures. At 298 K and 50 ppm of DIMC compound, the inhibition effectiveness is 57.81%. As the inhibitor concentration climbs to 300 ppm, the inhibition effectiveness rises to 91.48% (Table 3). The presence of the DIMC component in the pitting solution reduces the corrosion rate and so improves the inhibition efficiency. The corrosion process of LCS in oxygenated acidic chloride solutions can be summarized as follows:[35].

3.2.2 The effect of temperature. The temperature dependence of corrosion rate and inhibition efficiency was assessed over 298–328 K (see Table 2). As anticipated, corrosion rates increased with temperature in both the uninhibited and DIMC-inhibited systems, reflecting the higher mobility of electrolyte species (notably H^+) and the enhanced desorption of protective films driven by vigorous hydrogen evolution. Despite this thermal acceleration, DIMC retained strong performance: at 298 K and 300 ppm, an observable yet controlled reduction in efficiency is seen upon heating, from 91.48% (298 K) to 81.11% (328 K) ($\Delta \approx 10.37$ percentage points), consistent with partial desorption of adsorbates and the acceleration of hydrogen evolution at elevated temperature.

Table 2 Data of weight loss measurements at 360 min for carbon steel in 0.5 mol per L HCl in the absence and presence of different concentrations of compound DIMC, at different temperatures

DICA											
298 K			308 K			318 K			328 K		
C. (ppm)	θ	% IE	C. (ppm)	θ	% IE	C. (ppm)	θ	% IE	C. (ppm)	θ	% IE
0	—	—	**0**	—	—	**0**	—	—	**0**	—	…
50	0.58	57.81	**50**	0.52	52.23	**50**	0.49	48.92	**50**	0.47	46.85
100	0.64	64.06	**100**	0.56	56.71	**100**	0.55	54.67	**100**	0.51	53.85
150	0.72	71.88	**150**	0.70	70.14	**150**	0.66	66.18	**150**	0.62	62.23
200	0.79	78.51	**200**	0.74	74.25	**200**	0.71	71.22	**200**	0.68	68.53
250	0.85	85.00	**250**	0.82	82.08	**250**	0.78	78.06	**250**	0.75	75.17
300	0.92	91.48	**300**	0.85	85.07	**300**	0.83	83.09	**300**	0.81	81.11

More than 80% of the surface was still protected under aggressive acidic conditions. These outcomes imply that DIMC sustains appreciable surface coverage even at elevated temperatures. The notable yet controlled reduction in efficiency with temperature is consistent with a modest decline in adsorption strength—most plausibly due to partial desorption—while the overall response aligns with a mixed adsorption picture featuring strong physisorption complemented by partial chemisorption. Collectively, the data support the conclusion that DIMC remains a robust corrosion inhibitor under thermally demanding conditions.

3.2.3 Corrosion kinetics. Arrhenius and transition-state equations are used to estimate the activation parameters, such as activation energy (E_a^*), enthalpy change (ΔH_a^*), and entropy change (ΔS_a^*) for the dissolution of LCS in a 0.5 mol per L HCl solution in the absence and presence of various concentrations of the DIMC inhibitor.[10,36]

Arrhenius equation (eqn (3)):

$$\ln k = \ln A - E_a/RT \quad (3)$$

Transition state equation (eqn (4)):

$$\ln(k/T) = \ln(R/Nh) + \Delta S^*/R - \Delta H^*/RT \quad (4)$$

In the kinetic expressions employed here, k denotes the corrosion rate, A is the pre-exponential (frequency) factor, R is the universal gas constant, N is Avogadro's number, T is the absolute temperature, and h is Planck's constant. Fig. 3 presents the Arrhenius plots ($\log k$ *vs.* $1/T$) for LCS in the blank electrolyte and in the presence of various DIMC concentrations. The data exhibit high linearity with $R^2 \approx 0.99$, indicating excellent quality and reliability of the fits. From these linear regressions, the slopes and intercepts provide the magnitudes of (E_a^*) and A, respectively. Notably, the activation energy (E_a) increases upon inhibitor addition—consistent with an adsorption-induced energy barrier that impedes the corrosion process.

Table 4 Activation parameters for dissolution of CS in absence and presence of different doses of the compound DIMC in 0.5 M HCl

C (ppm)	E_a^* kJ mol^{-1}	R^2	ΔH^* kJ mol^{-1}	$-\Delta S^*$ J mol^{-1} K^{-1}
Blank	9.80	0.999	10.4	169
50	10.10	0.999	15.9	185
100	10.30	0.999	15.5	187
150	10.40	0.999	16.6	182
200	10.90	0.999	17.4	189
250	10.70	0.999	18.2	190
300	11.10	0.999	18.9	187

Specifically, E_a = 9.80 kJ mol^{-1} for the uninhibited system, rising to 11.10 kJ mol^{-1} at 300 ppm DIMC (see Table 4), thereby corroborating the inhibitor's protective action.

Complementary transition-state analysis ($\log k/T$ *vs.* $1/T$) yields the activation enthalpy (ΔH^*) and activation entropy (ΔS^*), offering additional thermodynamic insight into the inhibition mechanism (Fig. 3, right; Table 4). As summarized in Table 4, the (ΔS_a^*) values for LCS are negative in both the absence and presence of DIMC, implying that the activated complex at the metal/solution interface is more ordered—a hallmark of an adsorbed inhibitor–metal ensemble.[16,18] In parallel, (ΔH_a^*) shows a positive shift for LCS with and without different DIMC concentrations (Table 4 and Fig. 3, right), reflecting an endothermic activation process; this observation is consistent with the experimentally observed decline in inhibition efficiency at higher temperatures, where elevated thermal energy promotes partial desorption of the protective layer.[37,38] These kinetic and thermodynamic trends align well with the reported behavior of organic corrosion inhibitors in acidic chloride media.

To further probe interfacial stability, open-circuit potential (OCP) measurements were recorded for LCS in 0.5 mol per L HCl with and without varying DIMC concentrations. As shown

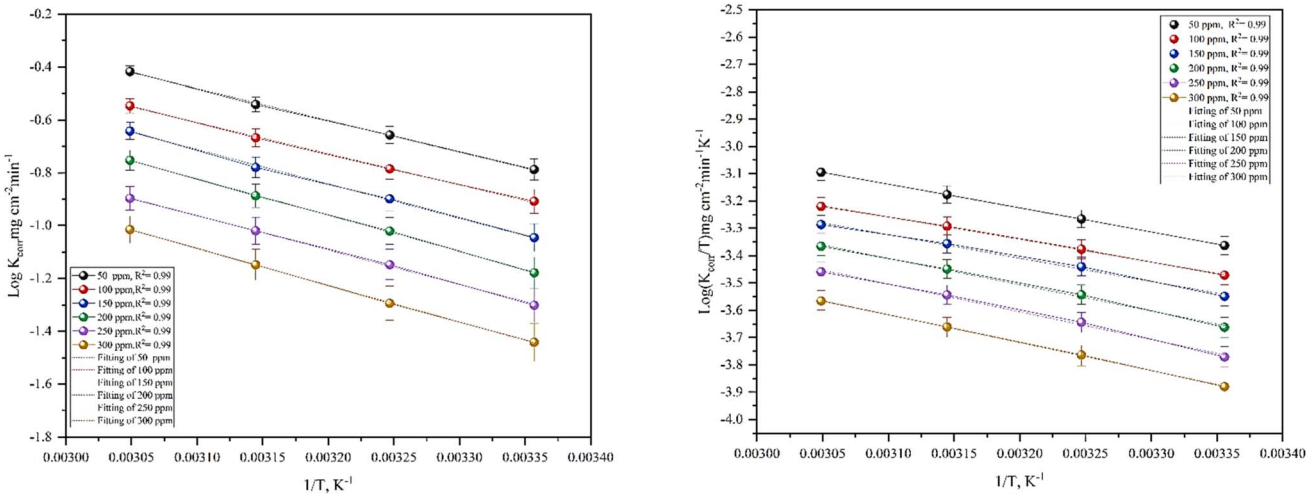

Fig. 3 Arrhenius plots (left) ($\log k$ *vs.* $1/T$) and transition-state plots (right) ($\log k/T$ *vs.* $1/T$) for the corrosion of LCS in 0.5 mol per L HCl without and with different concentrations of the DIMC compound.

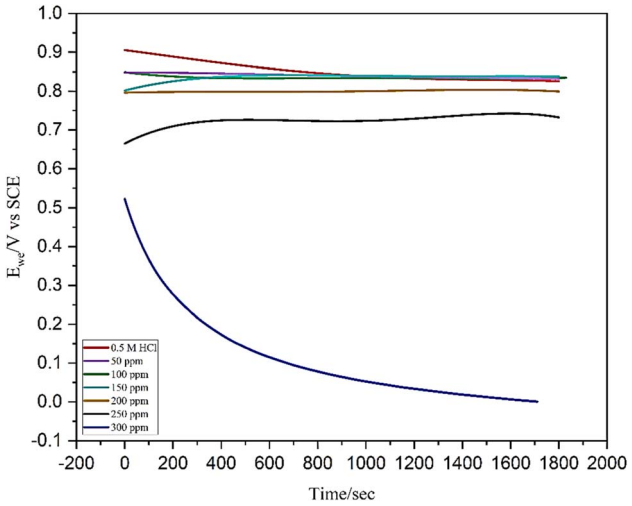

Fig. 4 Open circuit potential *versus* time curves of LCS in 0.5 mol per L HCl without and with different concentrations of the DIMC compound at 298 K.

in Fig. 4, the OCP curves shift to more positive potentials as DIMC concentration increases, a response indicative of enhanced protection and suppressed corrosion activity at the steel surface.

3.2.4 Adsorption isotherm. The adsorption behavior of the DIMC inhibitor on the surface of low carbon steel (LCS) was analyzed using weight loss data and interpreted through various isotherm models, including Langmuir, Temkin, Frumkin, Flory–Huggins, and Freundlich.[39] Among these, the Langmuir adsorption isotherm (eqn (5)) provided the best fit, suggesting monolayer adsorption of the synthesized compound on the LCS surface.

$$\frac{C}{\theta} = \frac{1}{K_{ads}} + C \tag{5}$$

Here, C is the inhibitor concentration, K_{ads} is the equilibrium constant of adsorption, and θ denotes the surface coverage. Fig. 2 shows the C/θ *vs.* C plots, which exhibit strong linearity with $R^2 \approx 0.9999$. The slight deviations of the slopes from unity are attributed to lateral interactions among adsorbed molecules.[21,22] The value of K_{ads} was obtained from the reciprocal of the intercepts of the linear fits in Fig. 2, and the calculated constants are compiled in Table 5. Higher K_{ads} values indicate the formation of a stable, strongly adherent inhibitor film on the LCS surface.[37] As temperature increases up to 318 K, K_{ads} declines—signaling reduced adsorption strength—while a subsequent rise at 328 K suggests a change in adsorption behavior. This trend is consistent with enhanced desorption of DIMC at moderate temperatures where physisorption predominates, followed at higher temperature by stronger interactions compatible with chemisorption, thereby increasing K_{ads}.[26,28] As previously noted, K_{ads} is directly related to the standard Gibbs free energy of adsorption (ΔG°_{ads}), which was calculated using eqn (6).[40,41]

$$K_{ads} = \exp\left(\frac{-\Delta G^{\circ}_{ads}}{RT}\right) \tag{6}$$

In this relation, R is the universal gas constant and T the absolute temperature. The computed standard Gibbs free energies of adsorption (ΔG°_{ads}) for DIMC over 298–328 K are summarized in Table 4. The negative ΔG_{ads} values demonstrate that DIMC adsorption onto the LCS surface is spontaneous and thermodynamically favorable across the entire temperature window. Prior reports commonly distinguish adsorption modes using (ΔG°_{ads}) thresholds [25,26] values more positive than −20 kJ mol^{-1} are typically associated with physisorption dominated by relatively weak electrostatic interactions, whereas values more negative than −40 kJ mol^{-1} are indicative of chemisorption involving partial charge sharing or transfer. For the present system, (ΔG°_{ads}) = −28.7 to −34.2 kJ mol^{-1}, placing DIMC squarely in the intermediate regime. This range strongly suggests a mixed adsorption mechanism—with contributions from both physisorption and chemisorption—rather than a single, exclusive mode.[42,43]

3.2.5 Potentiodynamic polarisation (PDP) measurements. Fig. 5 depicts the PDP curves for carbon steel in 0.5 mol per L HCl solution with and without varying doses of DIMC at 25 °C

Table 5 Equilibrium constant K_{ads} and standard free energy $\Delta G°_{ads}$ of adsorption of the DIMC on LCS in 0.5 M HCl at different temperatures

DIMC				
	$K \times 10^3$, mg. m^{-2} min^{-1} at 360 min			
C (ppm)	298 K	308 K	318 K	328 K
Blank	128.0	134.0	139.0	143.0
50	54.00	64.00	71.00	76.00
100	46.00	58.00	63.00	66.00
150	36.00	40.00	47.00	54.00
200	27.50	34.50	40.00	45.00
250	19.20	24.00	30.50	35.50
300	10.94	20.00	23.50	27.00

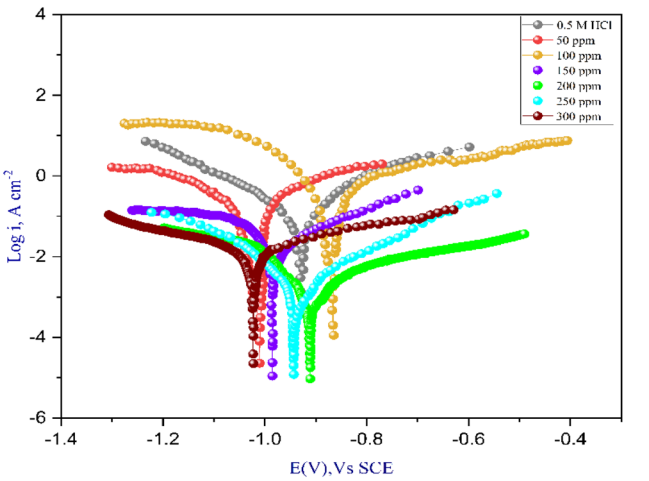

Fig. 5 Plots of potentiodynamic polarization measurements for dissolution of CS without and with different concentrations of compound DIMC, at 25 °C.

Table 6 Carbon steel corrosion rate after immersion in 0.5 mol per L HCl with and without different concentrations of the DICA compound at different temperatures

DIMC					
Temp, (K)	Slope	Intercept 10^2	$K_{ads}\times 10^3$ (mol^{-1})	$-\Delta G^0$ (kJ mol^{-1})	R^2
298	1.04	12.15	0.0502	34.2	0.999
308	1.02	14.81	0.0525	31.1	0.999
318	1.02	16.28	0.0665	29.8	0.999
328	1.01	18.33	0.0725	28.7	0.999

(50 to 300 ppm). Table 6 compiles electrochemical characteristics such as corrosion potential (E_{corr}), corrosion current density (I_{corr}), anodic and cathodic Tafel slopes, and IE to better understand the kinetics of carbon steel dissolving. Eqn (7) was used to get the IE% values for DIMC.

$$\text{IE }\% = \left(\frac{I_{corr} - I_{inh}}{I_{corr}}\right) \times 100 \quad (7)$$

The corrosion current densities—i_{corr} for the uninhibited electrolyte and i_{inh} in the presence of inhibitor—expressed in mA cm^{-2}, were determined by extrapolating the linear Tafel regions of both the cathodic and anodic branches back to the corrosion potential (E_{corr}). As the DIMC concentration increases, the polarization curves exhibit a dose-dependent shift of both branches toward lower current densities; importantly, the magnitude of this suppression intensifies with concentration. Quantitatively, introducing DIMC decreases i_{corr} from 155 mA cm^{-2} in the blank solution to 12 mA cm^{-2} at 300 ppm, clearly demonstrating that, in a strongly acidic medium, the inhibitor strongly attenuates cathodic hydrogen evolution as well as anodic iron dissolution.

The broader profile of the polarization curves, coupled with the concurrent reduction in cathodic and anodic currents, is consistent with the development of a compact, adsorbed protective film that hampers charge transfer across the interface. Such a film is expected to nucleate and grow preferentially at high-energy surface sites—for example, grain boundaries, inclusions, and defect regions—where electron–transfer reactions are most active. From a molecular perspective, adsorption is plausibly mediated by the π-electron system of the aromatic framework together with the lone pairs on nitrogen and sulfur within the hydrazide/thioamide moieties. These features enable donor–acceptor interactions with vacant Fe d orbitals, while protonation under acidic conditions can additionally promote electrostatic attraction, jointly accounting for the observed mixed-mode (physisorption/chemisorption) behavior. This mechanistic picture is fully aligned with recent reports on quinoline- and hydrazide-based inhibitors, which likewise achieve mixed-type inhibition *via* surface-film formation and electron-donating interactions at the steel interface.

As compiled in Table 7, the Tafel slopes (β_a and β_c) display only modest variations upon adding DIMC, indicating that adsorption primarily blocks reactant access (HCl) and reduces active-site availability rather than fundamentally altering the elementary corrosion pathways. Consistent with a mixed-type response, the shifts in E_{corr} do not follow a monotonic trend with concentration, and the maximum $\Delta E_{corr} \approx 77$ mV remains within ±85 mV, the customary threshold for classifying an inhibitor as mixed-type. Taken together—the bilateral decrease in current densities, the limited changes in β_a/β_c, and the bounded E_{corr} displacement—these results confirm that DIMC acts on both the cathodic hydrogen-evolution and anodic metal-dissolution reactions, increasing IE values and corroborating the OCP evidence for mixed-type inhibition.[31–33]

3.3 Electrochemical impedance spectroscopy (EIS)

Fig. 6 displays the Nyquist plots for the corrosion of the LCS working electrode in 0.5 mol L^{-1} HCl, recorded with and without DIMC at inhibitor concentrations spanning the studied range, over the potential window −1400 to −350 mV and the frequency domain 100 kHz to 50 Hz. In the absence of inhibitor molecules, the spectra exhibit two distinct (depressed) capacitive loops, a hallmark response commonly attributed to the buildup of an insoluble oxide/corrosion-product film on the steel surface that introduces multiple interfacial time constants.[34,35] By contrast, upon introducing the synthesized DIMC into the aggressive electrolyte, the impedance response of carbon steel is significantly altered (see Table 8), providing clear electrochemical evidence of the compound's inhibitory action. Specifically, the diameter of the capacitive loops increases progressively with successive additions of DIMC, indicating

Table 7 Potentiodynamic polarization parameters of CS in 0.5 mol per L HCl containing different concentrations of the compound DIMC at 25 °C

DIMC						
C (ppm)	$-E_{corr}$ (mV *vs.* SCE)	βa (mV dec^{-1})	βc (-mV dec^{-1})	I_{corr} (mA cm^{-2})	θ	IE%
Blank	950	6.40	4.96	0.155	—	—
50	1010	6.42	9.65	0.078	0.497	49.67 ± 0.20
100	880	7.74	12.44	0.060	0.613	61.29 ± 0.10
150	985	4.66	6.85	0.036	0.768	76.77 ± 0.25
200	911	3.15	3.46	0.031	0.800	80.00 ± 0.15
250	943	4.24	7.22	0.023	0.850	85.00 ± 0.20
300	1023	3.10	6.15	0.012	0.922	92.25 ± 0.10

Table 8 EIS data of CS in 0.5 mol per L HCl in the absence and presence of different concentrations of the DICA compound at 25 °C

DIMC				
C (ppm)	R_{ct} (Ω cm^2)	C_{dl} (F cm^{-2}) $\times 10^{-6}$	θ	IE%
Blank	110	140.0	—	—
50	292	128.0	0.623	62.32 ± 0.04
100	385	101.0	0.714	71.42 ± 0.06
150	595	82.0	0.815	81.51 ± 0.07
200	925	68.0	0.881	88.10 ± 0.08
250	1080	47.0	0.895	89.51 ± 0.10
300	1290	22.0	0.915	91.50 ± 0.10

a steady increase in charge-transfer resistance (R_{ct}) as a protective interfacial layer develops and consolidates on the steel surface.

To interpret this behavior, it is useful to recall that the Nyquist arc diameter in an EIS spectrum is inversely related to the rate of charge transfer at the metal/electrolyte boundary; hence, a larger semicircle directly reflects a higher R_{ct}, which in turn signifies a slower rate for the electrochemical steps governing corrosion. In practical terms, larger arcs are typically associated with the formation of an insulating/adsorbed film that impedes the ingress of aggressive ionic species and suppresses electron/ion exchange at the interface. In the present system, the monotonic growth of the arc diameter with inhibitor concentration for DIMC points to the progressive establishment of a denser, more coherent, and more stable adsorbed layer, which concurrently attenuates both anodic metal-dissolution and cathodic hydrogen-evolution pathways. This mechanistic interpretation is fully consistent with widely accepted models for inhibitor-film behavior in strongly acidic chloride environments and corroborates the performance trends derived from the complementary techniques employed in this study. In particular, the capacitive loop at 300 ppm is considerably broader than that observed at 50 ppm, underscoring the direct relationship between surface coverage and charge-transfer suppression at higher DIMC loadings.

The Bode representations in Fig. 7 reinforce these conclusions. As the DIMC concentration is increased, the impedance modulus ($|Z|$) is enhanced across the entire frequency spectrum, with especially pronounced gains at low frequencies, where interfacial blocking effects dominate the overall response. Simultaneously, the phase angle undergoes a shift toward more negative values at intermediate (mid) frequencies, signaling a more capacitive interfacial character associated with well-formed adsorbed films.[36] In aggregate, the observed increases in $\log|Z|$ and the more negative phase angles track the greater degree of adsorption and improved film continuity that arise as additional DIMC molecules anchor to the carbon-steel surface. These spectral evolutions are in line with the inhibitor's role in thickening/strengthening the interfacial barrier and stabilizing the double-layer structure.

For quantitative analysis, the EIS spectra of the DIMC-containing systems were fitted using an appropriate equivalent circuit (Fig. 8), comprising the solution resistance (R_s), the double-layer capacitance (C_{dl}), and the charge-transfer resistance (R_{ct}).[39] The extracted electrochemical parameters describing the corrosion of carbon steel in 0.5 mol per L HCl in the absence and presence of the inhibitor—namely C_{dl}, R_{ct}, and the EIS-based inhibition efficiency (IE%)—were computed following eqn (8),[40–44] and the complete set of values is summarized in Table 8. Consistent with the qualitative trends in the Nyquist and Bode plots, the fits reveal R_{ct} increases and C_{dl} decreases with rising DIMC concentration, reflecting reduced charge transfer, lower effective interfacial capacitance (due to thicker/less dielectric double layers and/or decreased active area), and enhanced barrier properties of the inhibitor

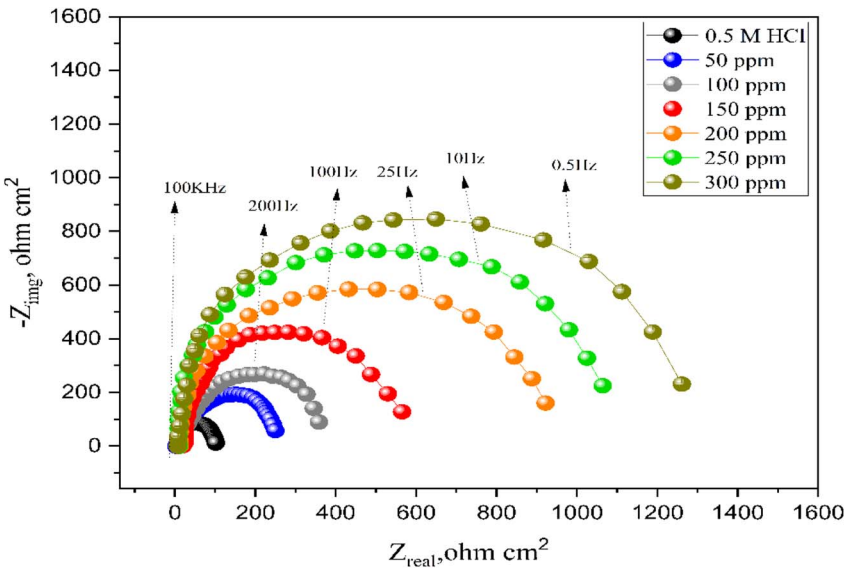

Fig. 6 Plot of Nyquist impedance spectroscopy measurements for dissolution of CS without and with different concentrations of compound DIMC, at 25 °C.

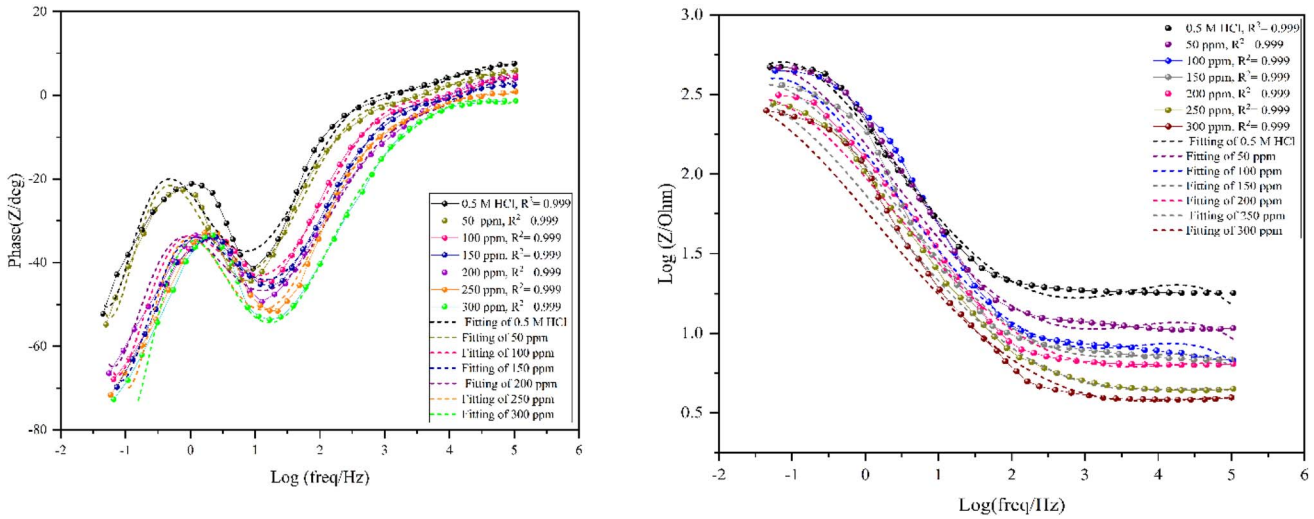

Fig. 7 The Bode plots left and right for the corrosion of LCS in 0.5 mol per L HCl without and with different concentrations of the DIMC compound at 25 °C.

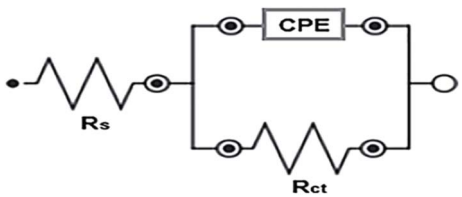

Fig. 8 Equivalent circuit model used to fit experimental EIS data.

film. Collectively, the frequency-resolved signatures (Fig. 6–7), the circuit-based descriptors (Fig. 8), and the tabulated parameters (Table 8) converge to demonstrate that DIMC suppresses corrosion by forming and consolidating an adsorbed protective layer which effectively retards both anodic and cathodic processes within the examined potential and frequency windows.

$$\mathrm{IE_{EIS}}\% = \left(1 - \left(\frac{R_{ct}}{R_{ct\ inh}}\right) \times 100 = \theta \times 100\right) \quad (8)$$

3.4 Surface morphology

3.4.1 Scanning electron microscope. Fig. 9–11 present SEM micrographs of low-carbon steel after immersion in 0.5 M HCl in the absence and presence of DIMC. The uninhibited specimen (Fig. 9) displays hallmark features of severe acid corrosion—pronounced pitting, intergranular cracking, and heterogeneous topography indicative of extensive surface degradation. These morphological observations are consistent with the electrochemical and gravimetric metrics for the blank: a low R_{ct} and elevated C_{dl} in the EIS data together with a high corrosion rate from WL measurements, all of which confirm the lack of an effective barrier film on the steel surface.

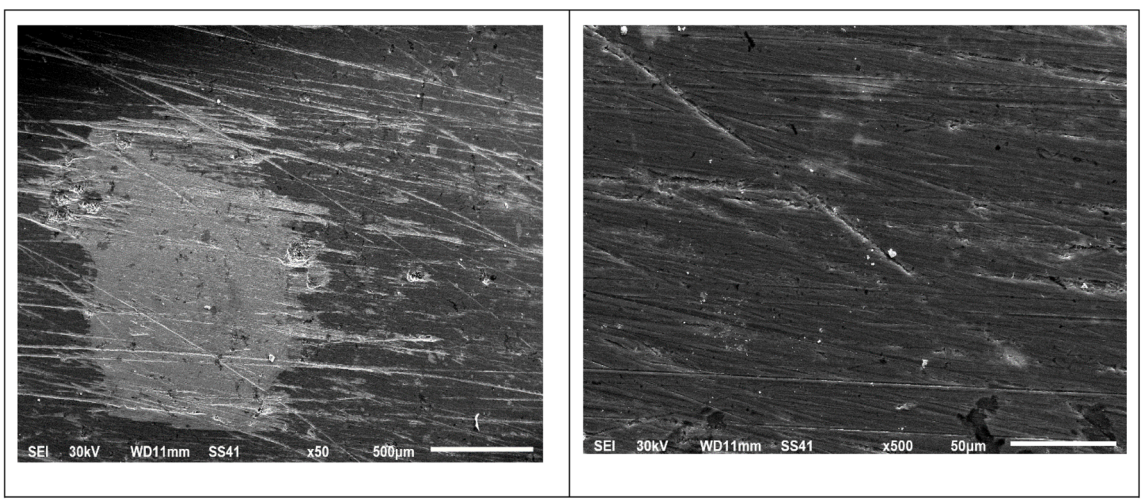

Fig. 9 SEM image of pure LCS after polishing at 50 and 500 µm.

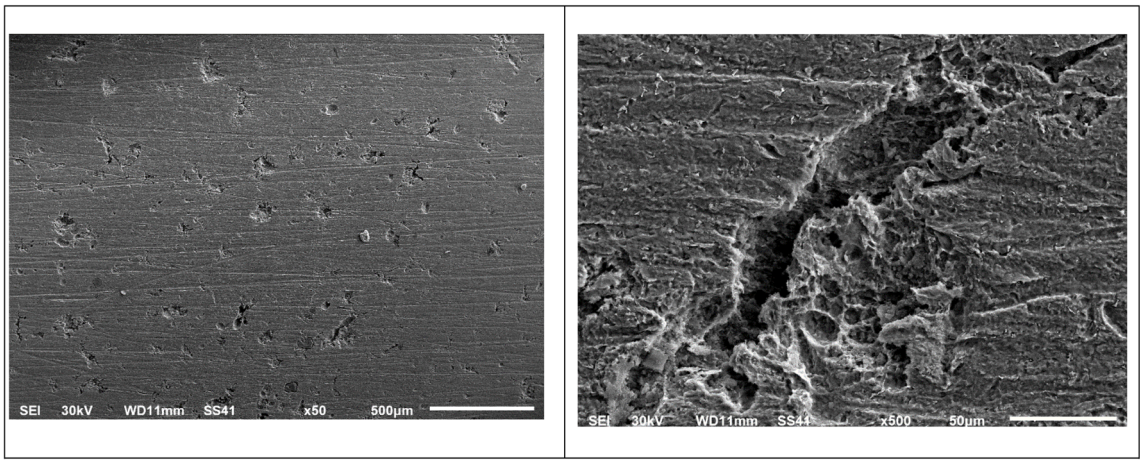

Fig. 10 SEM image of LCS after immersing in 0.5 mol per L HCl (50 & 500 µm).

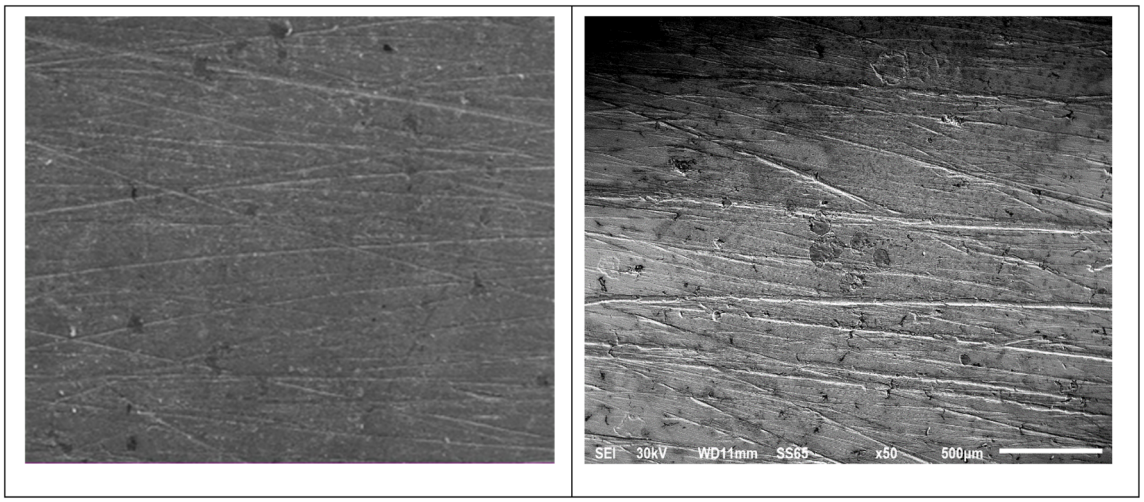

Fig. 11 SEM image of LCS after immersing in 0.5 mol per L HCl + 300 ppm of DIMC (50 & 500 µm) exhibiting a smoother morphology and reduced corrosion damage.

In sharp contrast, the surface exposed to 300 ppm DIMC (Fig. 11) appears smoother, more homogeneous, and largely free of localized attack, with only minimal vestiges of pits or fissures. The visual suppression of damage correlates with the increase in R_{ct} and the marked reduction in corrosion rate, supporting the formation of a robust inhibitor film. This protective layer is plausibly generated by adsorption of DIMC at active surface sites, which blocks catalytic centers for dissolution and retards the ingress/diffusion of aggressive H^+ ions, thereby dampening both anodic and cathodic interfacial reactions. At intermediate concentration (Fig. 10), the images reveal partial coverage—a patchier film with moderate surface relief—mirroring the dose-dependent rise in inhibition efficiency observed electrochemically.

Taken together, the SEM evidence visually corroborates the conclusions drawn from EIS and weight-loss testing, offering direct morphological confirmation of DIMC's surface-protection mechanism. The improved uniformity and continuity of the inhibited surface are consistent with a mixed physisorption–chemisorption adsorption mode: DIMC builds a compact barrier that limits charge transfer, stabilizes surface energy, and prevents corrosive attack under the examined acidic conditions.

3.4.2 Atomic force microscope. To quantitatively assess the corrosion-inhibition morphology of LCS immersed in 0.5 mol per L HCl, Fig. 12–14 present AFM images acquired in the absence and presence of DIMC. The freshly abraded (polished) reference surface (Fig. 12) exhibits a very smooth topology prior to immersion; the root-mean-square height (S_q) measured on this specimen is 81.0 µm, reflecting the low-relief finish produced by the standard grinding/polishing sequence. In contrast, immersion in the uninhibited acid produces pronounced topographic degradation (Fig. 13): the LCS exposed to 0.5 mol per L HCl without DIMC shows a high roughness of 410 µm, consistent with corrosive attack and surface dissolution features typical of strong acids. When the optimal concentration of DIMC is introduced (Fig. 14), the LCS surface appears much more uniform and comparatively smooth, with

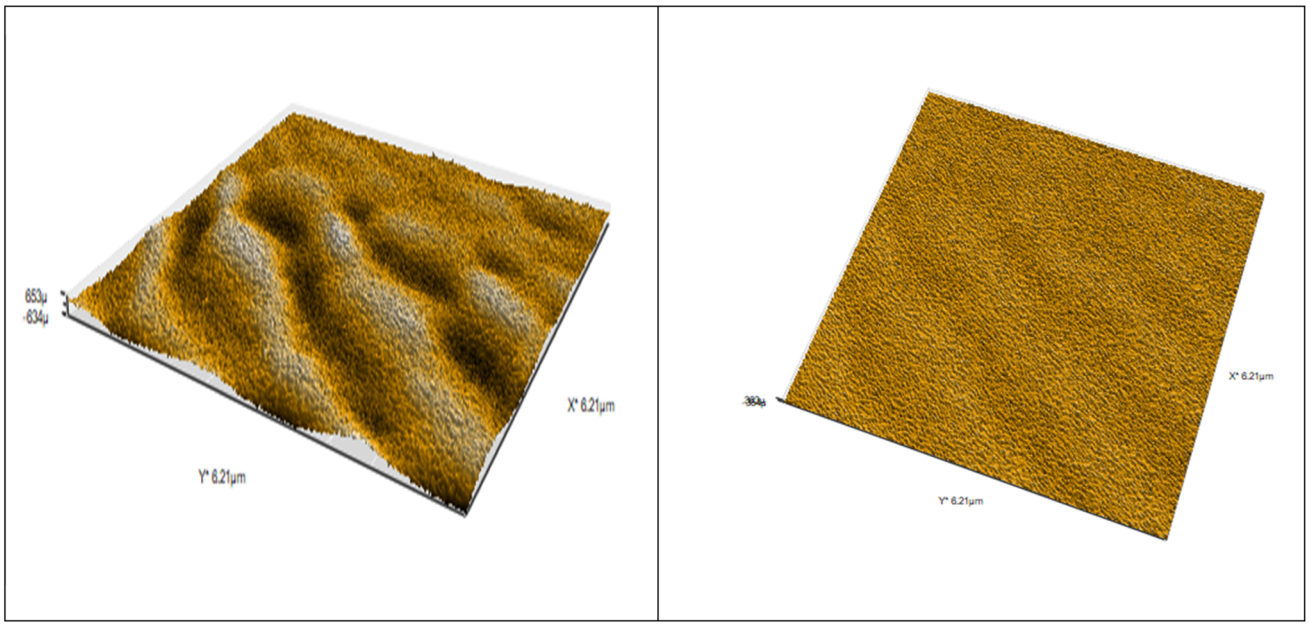

Fig. 12 AFM of pure LCS after polishing, in DIMC ting smoother surface and effective corrosion inhibition film formation.

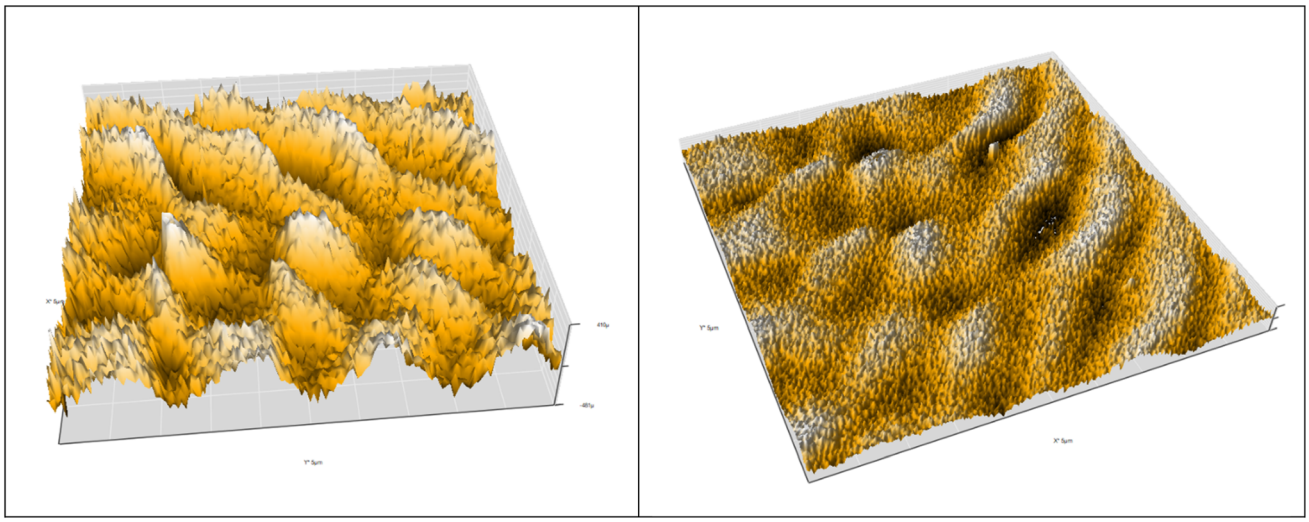

Fig. 13 AFM of LCS after immersing in 0.5 mol per L HCl.

an average surface height of 95.0 μm, indicating the development of a microscopically thin adsorbed coating attributable to the inhibitor. Comprehensive height parameters—arithmetic mean height (S_a), root-mean-square height (S_q), maximum peak height (S_p), maximum pit height (S_v), and maximum height (S_z)—are tabulated in Table 9 in micrometers, evaluated in accordance with ISO 25178 standards.[45,46]

The reduction in roughness from 410 μm (blank) to 95.0 μm (with DIMC) demonstrates that the inhibitor substantially suppresses surface degradation under acidic conditions. This improvement is attributed to the formation of a compact, continuous protective film by DIMC on the steel surface, which shields active sites and limits direct exposure of the substrate to the aggressive electrolyte. The smoother morphology observed in the AFM images directly supports the high inhibition efficiencies quantified *via* electrochemical (EIS/PDP) and gravimetric (WL) measurements, linking film formation to charge-transfer suppression and diminished mass loss. Collectively, the AFM results provide strong morphological evidence for effective film-based corrosion protection, reinforcing the proposed adsorption-driven mechanism of DIMC under the studied conditions.

3.5 DFT simulation and calculation

To elucidate the molecular–level interactions between DIMC and the carbon-steel (CS) surface, we carried out density

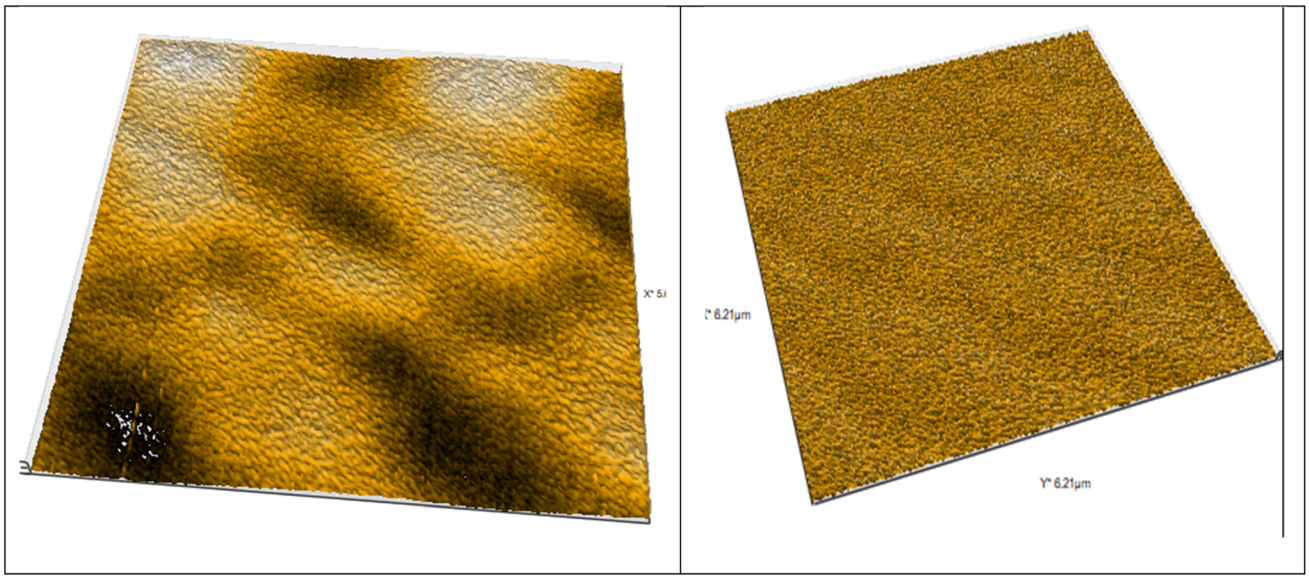

Fig. 14 AFM of LCS after immersing in 0.5 mol per L HCl + 300 ppm of DIMC.

Table 9 AFM of LCS surface parameters

Substance	S_a (μm)	S_q (μm)	S_p (μm)	S_v (μm)	S_z (μm)
Control	58	81	230	392	196
0.5 mol per L HCl	410	410	410	705	450
DIMC	78	95	285	420	232

functional theory (DFT) calculations. Geometry optimization and evaluation of key electronic properties were performed with the B3LYP exchange–correlation functional in conjunction with the 6-31G(d,p) basis set under gas-phase conditions to obtain the lowest-energy conformer and its associated frontier-orbital characteristics. In addition, complementary solution-phase computations were executed in aqueous media for both the neutral and protonated forms of the inhibitor to capture protonation-dependent electronic effects relevant to acidic environments. Fig. 15 displays the optimized molecular structure of DIMC together with its highest occupied molecular orbital (HOMO) and lowest unoccupied molecular orbital (LUMO) distributions.

Beyond frontier orbitals, a suite of reactivity descriptors that influence adsorption and charge-transfer at the metal interface—including ionization potential (I), electron affinity (A), electronegativity (χ), chemical potential (μ), hardness (η), softness (σ), electrophilicity (ω), and the total energy (E_t)—was derived from the DFT outputs using the corresponding relations (eqn (9)–(15)). The calculated values for all species and states considered are compiled in Table 10, providing a quantitative basis for interpreting DIMC's adsorption propensity and inhibitory behavior on the CS surface.

$$\Delta E = E_{LUMO} - E_{HOMO} \quad (9)$$

$$I = -E_{HOMO} \quad (10)$$

$$A = -E_{LUMO} \quad (11)$$

$$\mu = -\chi \quad (12)$$

$$\mu = \frac{(E_{HOMO} + E_{LUMO})}{2} \quad (13)$$

$$\eta = \frac{(E_{LUMO} - E_{HOMO})}{2} \quad (14)$$

$$\sigma = 1/\eta \quad (15)$$

Within the frontier molecular orbital (FMO) framework, the spatial distributions and energies of HOMO and LUMO enable identification of the adsorption-active centers that govern molecule–surface interactions. As shown in Fig. 15, the frontier orbitals of the DIMC inhibitor—together with the mapped lone-pair electron density, electrostatic potential, total electron density, and interaction potential—are predominantly concentrated around the heteroatoms N, S, and O. This localization pattern points to these heteroatomic sites as the primary anchoring centers during interaction with the LCS surface, consistent with an adsorption mechanism driven by donor–acceptor coordination between the inhibitor and metallic surface sites.[46] In this context, the E_{HOMO} and E_{LUMO} values are especially informative: E_{HOMO} reflects the inhibitor's electron-donating propensity toward partially vacant Fe 3d orbitals, whereas E_{LUMO} gauges its ability to accept back-donation from the metal, thereby stabilizing the adsorbate–substrate ensemble.[47,48]

The HOMO–LUMO energy gap ($\Delta E = E_{LUMO} - E_{HOMO}$) serves as a consolidated indicator of molecular reactivity, where smaller ΔE typically corresponds to enhanced chemical reactivity, greater electronic polarizability, and lower excitation barriers at the interface. According to Table 10, DIMC exhibits

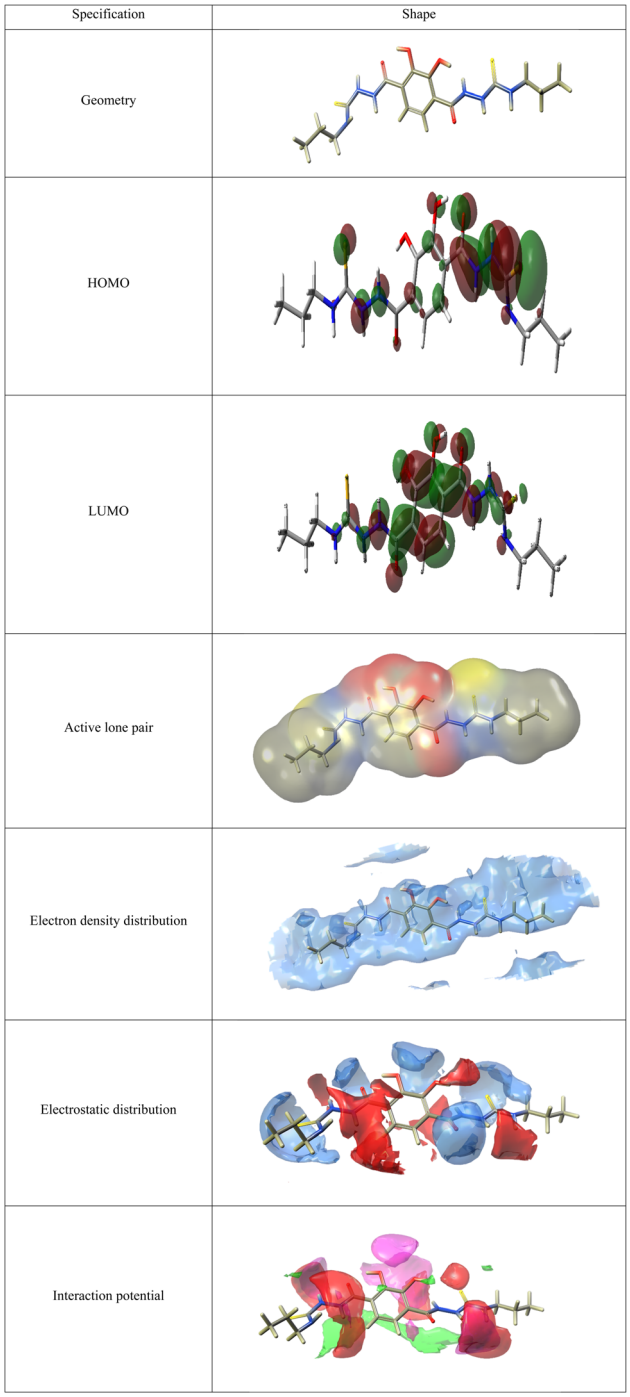

Fig. 15 Geometrical structure, active lone pair, interaction potential, electrostatic and charge density distribution of HOMO and LUMO levels of the inhibitor compound DIMC.

a low ΔE of 1.61 eV, underscoring favorable electronic characteristics for adsorption and charge-transfer mediation during inhibition. In parallel, the dipole moment (μ) captures molecular polarity and charge distribution, which also modulate adsorption strength and interfacial orientation. A larger μ generally implies stronger dipole–dipole and electrostatic interactions with the metallic surface; for DIMC, $\mu = 7.41$ D (Debye units) indicates a polarity level conducive to robust

Table 10 The calculated quantum chemical parameters obtained from DFT theory

Complex	DIMC	
Parameters	Values	Units
Stretching	31	kcal mol^{-1}
Bending	1720	kcal mol^{-1}
Stretch-bending	−2.1	kcal mol^{-1}
Torsion	52.5	kcal mol^{-1}
Dipole/dipole	−26.25	kcal mol^{-1}
HOMO	−5.76	eV
LUMO	−4.15	eV
Energy gap ΔE	1.61	eV
Dipole moment D_m	7.41	Debye
Ionization potential I	5.76	eV
Electron affinity A	4.15	eV
Hardness η	0.81	eV
Softness σ	1.24	eV
Chemical potential μ	−4.96	eV
Electronegativity χ	4.96	eV
Electrophilicity ω	15.25	eV
Total energy (E_t)	−2200	eV

adsorption under acidic conditions.[49] Complementing these trends, the descriptor set further reveals low hardness and high softness values for DIMC—signatures of enhanced responsiveness to external electric fields and a greater capacity to engage in donor–acceptor interactions with surface Fe sites.

Taken together, the DFT-derived descriptors—frontier-orbital localization on N/S/O centers, low ΔE, a meaningful dipole moment, and soft, low-hardness character—provide a coherent electronic rationale for the experimentally observed inhibition behavior. The computational picture aligns closely with the electrochemical metrics (PDP/EIS) and gravimetric results, indicating that the quantum-chemical properties of DIMC correlate strongly with its measured inhibition efficiency for LCS in acidic chloride media, in agreement with prior structure–activity relationships for organic inhibitors.[50]

4 In summary

DIMC exhibits a comparatively high E_{HOMO} together with a small HOMO–LUMO gap (ΔE), indicating pronounced electron-donor capability and elevated chemical reactivity—features that favor chemisorptive bonding interactions at the steel interface. Consistently, the molecular electrostatic potential (MEP) mapping highlights electron-rich loci centered on the N and O atoms of the hydrazide and hydroxyl functionalities, identifying these heteroatoms as the primary adsorption centers that can engage in donor–acceptor coordination with vacant Fe orbitals, in agreement with the frontier-orbital analysis.

The adsorption thermodynamics/stoichiometry are well captured by a Langmuir isotherm, which affords an excellent linear fit ($R^2 \approx 0.99$) and supports monolayer coverage on a nominally homogeneous surface, thereby reinforcing the DFT-derived picture of site-specific binding. The extracted

equilibrium constant (K_{ads}) and the standard Gibbs free energy of adsorption (ΔG°_{ads}) further indicate that the process is spontaneous and dominated by physisorption with a meaningful chemisorptive contribution, consistent with the mixed-mode adsorption scenario inferred from electronic descriptors.

These theoretical insights cohere with the experiments: the inhibitor delivers high protection efficiencies (up to 92.25%), while SEM and AFM micrographs reveal a continuous, stable adsorbed film that suppresses both anodic metal dissolution and cathodic hydrogen evolution. Collectively, the modeling and measurements converge on a mechanism in which DIMC produces a compact interfacial layer that limits charge transfer and reactant access, thereby curtailing corrosion under acidic conditions.

For external validation, this interpretation aligns with prior findings on hydrazide- and hydroxyl-substituted organic inhibitors, as discussed in the manuscript,[41–44] providing additional literature support for the mixed physisorption–chemisorption inhibition pathway proposed here.

4.1 Monte Carlo simulation

Monte Carlo (MC) simulation is a molecular-mechanics approach that uses simulated annealing for configurational optimization.[51] Relative to quantum-mechanical treatments, MC sampling is far less computationally intensive, enabling broader conformational searches at significantly lower time and cost. Because adsorption mode is strongly governed by molecular structure, MC simulations were deployed to probe both the adsorption behavior on the steel surface and the interaction mechanism between the DIMC inhibitor and the metallic substrate. Fig. 16 presents side- and top-view snapshots of the

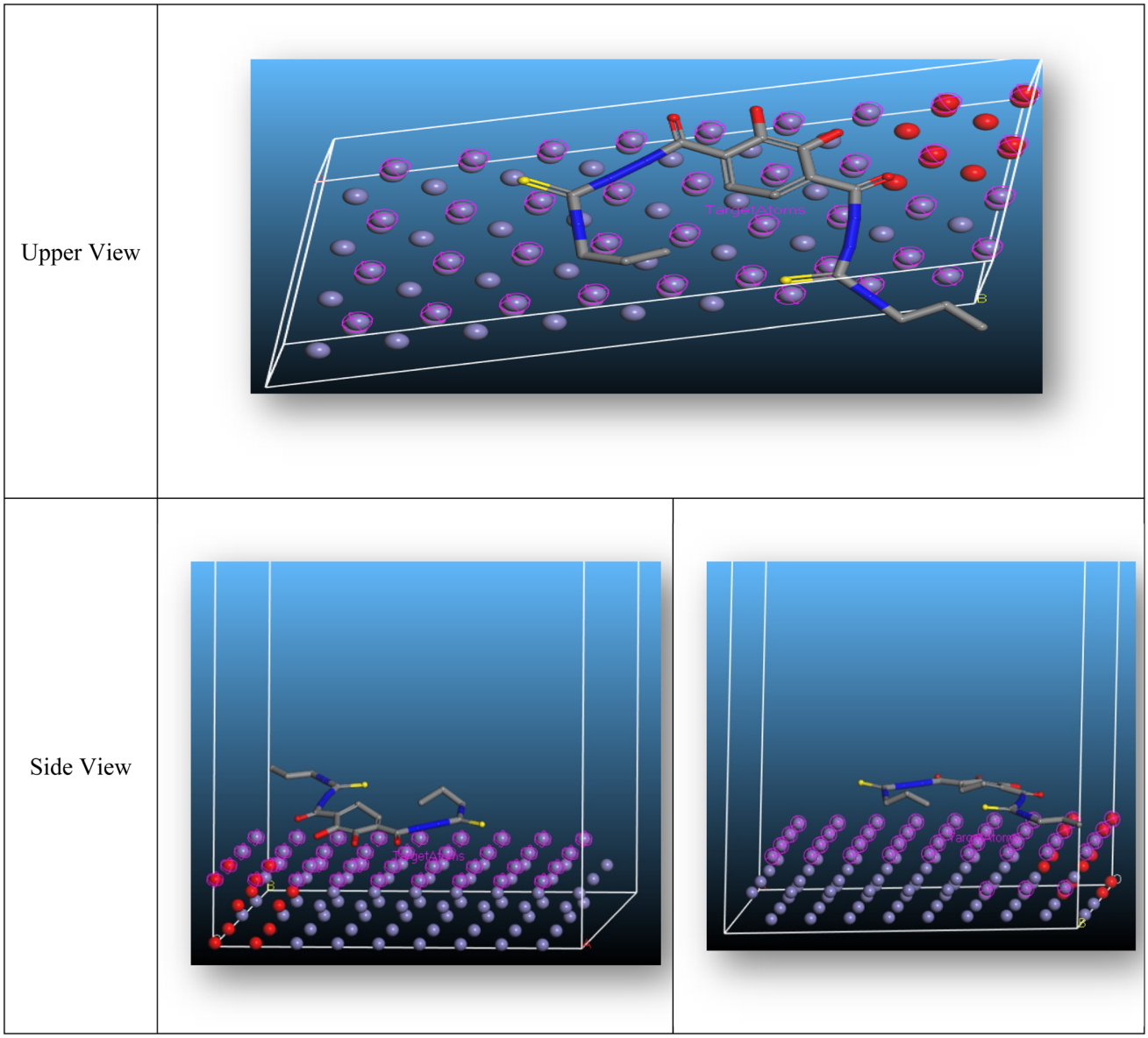

Fig. 16 Side view and top view for the adsorption of the DIMC inhibitor on LCS.

optimized adsorption geometries on the LCS surface, illustrating preferred orientations and surface coverage. The interaction (binding) energy between DIMC and LCS—used as a quantitative indicator of adsorption strength and film stability—was computed according to eqn (14), providing the basis for correlating calculated adsorption energetics with experimentally observed inhibition performance.

$$E_{ads} = E_{Fe\text{-}inh} - (E_{inh} - E_{Fe}) \quad (16)$$

In eqn (14), E_{inh} and E_{Fe} denote the total energies of the isolated inhibitor and the iron surface, respectively. As summarized in Table 11, the binding (adsorption) energy computed for DIMC on Fe is −690 kJ mol^{-1} by MC simulation, a markedly negative value that evidences strong, favorable adsorption and supports extensive interfacial coverage. This magnitude indicates that DIMC molecules adsorb to a substantial extent on the iron surface, promoting the formation of a thick, continuous film that enhances protection of LCS in 0.5 mol L^{-1} HCl.

Analysis of the optimized configurations shows that adsorption is anchored predominantly through the heteroatom-rich fragments—notably S, N, and O in the thioamide/carbonyl region—together with the phenyl π-system. These units provide donation/back-donation pathways and strong surface coupling, while the remaining portions of the molecule adopt a slanted (sloping) orientation over the interface, aiding lateral coverage and film consolidation. This topology reflects a high density of active donor sites per molecule, which rationalizes the strong inhibitory efficacy observed experimentally.

For the protonated inhibitor forms, the MC results indicate that the molecules tend to be situated above the iron surface with a more lifted orientation, yielding more limited lateral coverage than the neutral adsorbate. Consistent with adsorption thermodynamics, Table 11 also reports negative E_{ads} values, confirming that the DIMC–Fe interaction is spontaneous and that the inhibitor exhibits a high propensity to associate with the metallic surface.[52] Additionally, the total interaction energy of 185 kJ mol^{-1} further substantiates that DIMC–Fe(110) coupling occurs readily, in line with the trends in inhibition efficiency established by the electrochemical and quantum-chemical analyses presented in this work.

4.2 Mechanism of action

The results confirm that DIMC markedly suppresses the corrosion of low-carbon steel (LCS) in 0.5 mol L^{-1} HCl. To rationalize this performance, we consider the compound's functional architecture and its adsorption behavior at the metal/electrolyte interface. As shown in Fig. 9, DIMC presents multiple adsorption-competent motifs—carbonyl/thioamide (C═O/C═S) and hydrazine functionalities together with aromatic π-systems and hydroxyl groups—that can interact strongly with surface Fe sites. The ultimate inhibition efficiency depends on a constellation of factors: molecular size and conformation, nature and positioning of functional groups, the charge and electronic character of the metal surface under acidic conditions, and the electron-density distribution across the inhibitor framework.

Two complementary adsorption pathways are implicated: chemisorption and physisorption. In the chemisorptive route, neutral DIMC molecules displace interfacial water and establish coordination bonds by donating lone-pair electrons (N, O, and S centers) into vacant Fe d-orbitals. Concurrently, back-donation from filled Fe d-states into the π-system of DIMC—especially the aromatic ring network—can stabilize the adsorbed ensemble (*i.e.*, retro-donation), strengthening metal–inhibitor coupling and consolidating the interfacial film.

In strongly acidic media, a fraction of DIMC exists in protonated form. Direct approach of cationic species to the positively polarized LCS surface (in the presence of H_3O^+) can be electrostatically disfavored. However, chloride ions (Cl^-)—which are weakly hydrated and accumulate at the interface—create localized negative patches that foster electrostatic attraction of protonated DIMC. The result is physisorption *via* ion–dipole and coulombic interactions, enabling meaningful surface coverage even when chemisorption is partially impeded. The combined outcome is a dual-mode adsorption scenario, wherein chemical bonding and electrostatic attachment operate in parallel to generate a compact, protective layer that restricts charge transfer and limits reactant ingress. This integrated mechanism is schematically summarized in Fig. 17.

4.2.1 Comparative discussion with recent literature. The inhibition performance of DIMC was contextualized against recent heterocyclic/quinoline systems reported between 2022 and 2024. Galai *et al.* (2024)[53] documented a quinoline-based inhibitor achieving ∼89% protection at 500 ppm in 1 M HCl, supported by EIS, SEM, and Monte Carlo analyses that evidenced a mixed-adsorption mechanism. In a related vein, Abouchane *et al.* (2022)[54] reported 90–92% efficiency for quinoline-3-carboxylate derivatives at 303 K, with electrochemical signatures and HOMO–LUMO characteristics comparable to other high-performing organics. Against these benchmarks, DIMC delivered 91.41% inhibition at only 300 ppm and 298 K, underscoring both high efficacy at lower dosage and a strong chemisorptive affinity for the LCS surface under acidic conditions. Furthermore, Ech-chebab *et al.* (2022)[55] and Dahmani *et al.* (2024)[56] highlighted how donor heteroatoms (N, S, O) and delocalized π-systems enhance adsorption—fully consistent with DIMC's electron-rich architecture, as corroborated by our DFT results and MEP mapping that localize active adsorption centers on the heteroatom sites.

Table 11 The descriptors calculated by the Monte Carlo simulation for adsorption of the inhibitor *n* the LCS surface

Molecule	Total energy (kJ mol^{-1})	Adsorption energy (kJ mol^{-1})	Deformation energy (kJ mol^{-1})	Rigid adsorption energy (kJ mol^{-1})
DIMC	185	−690	−390	−300

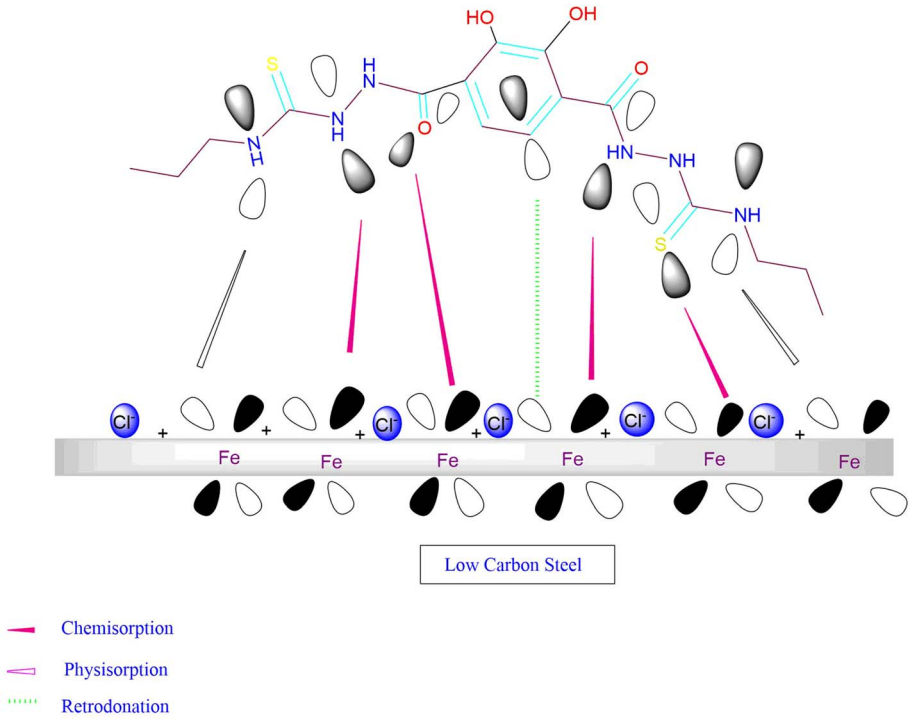

Fig. 17 Interaction mechanism of DIMC compound with the LCS surface.

Convergence with broader literature is also evident: Oubaaqa *et al.* (2022),[57] Dahmani *et al.* (2022),[58] and Ech-chebab *et al.* (2023)[59] emphasized the diagnostic value of surface-roughness attenuation and rigorous EIS fitting in validating inhibitor performance—both of which are satisfied by DIMC's multi-technique dataset. Collectively, this comparison shows that DIMC not only matches or exceeds reported efficiencies under similar conditions but also stands out as a credible green alternative, supported by a coherent, cross-validated electrochemical, morphological, and computational evidence base.

5 Conclusions

In this work, we synthesized a resorcinol-based hydrazinecarbothioamide derivative, DIMC, and rigorously assessed its performance as a corrosion inhibitor for low-carbon steel (LCS) in 0.5 M HCl. The inhibitor delivered high protection efficiencies, attaining 91.48% at 298 K and retaining 81.11% at 328 K, evidencing both thermal robustness and resilient surface adsorption under increasingly harsh conditions.

Electrochemical diagnostics (PDP and EIS) establish that DIMC operates as a mixed-type inhibitor, simultaneously suppressing anodic metal dissolution and cathodic hydrogen evolution. Gravimetric weight-loss measurements are consonant with these electrochemical trends, reinforcing internal consistency across methods. Complementary SEM and AFM imaging demonstrate pronounced mitigation of topographical damage and a marked reduction in roughness, consistent with the formation of a protective interfacial film. Furthermore, DFT calculations and Monte Carlo adsorption simulations rationalize the experimental behavior, indicating a dual physisorption–chemisorption pathway and strong molecule–surface interactions that stabilize coverage.

Taken together, the combined evidence shows that DIMC builds a stable, adherent barrier layer on LCS that remains effective in aggressive acidic media. Its measured efficacy, rational molecular design, and compatibility with environmental considerations position DIMC as a credible candidate for industrial deployment, notably in acidizing operations in the oil and gas sector and other workflows that involve sustained exposure to strong mineral acids.

Author contributions

Mostafa A. A. Mahmoud – conceptualization; methodology; investigation; formal analysis; visualization; writing – original draft; writing – review & editing; supervision; project administration. Sherin A. M. Ali – methodology (electrochemical testing and impedance fitting); validation; formal analysis; visualization; writing – review & editing. Mostafa E. Salem – software (DFT/Monte Carlo setup and post-processing); data curation; formal analysis (computational); writing – review & editing. Mansour Alsarrani – resources (laboratory facilities and chemicals); supervision; writing – review & editing. Mohamed Abdel-Megid – software (dft modeling and mep/homo–lumo visualization); visualization; writing – review & editing. H. A. El Nagy – investigation (synthesis/characterization; SEM/AFM sample prep); resources; data curation. Ahmed Z. Ibrahim – resources (industrial materials/context); validation; writing – review & editing.

Conflicts of interest

There are no conflicts to declare.

Data availability

All data generated or analyzed during this study are included in this published article.

Acknowledgements

This work was supported and funded by the Deanship of Scientific Research at Imam Mohammad Ibn Saud Islamic University (IMSIU) (grant Number IMSIU-DDRSP2502).

References

1 M. M. Kamel, S. M. Rashwan, M. A. A. Mahmoud, S. A. A. El-Mekawy, M. K. Awad and H. E. Ibrahim, An eco-friendly Resorcinol Derivative as An inhibitor for Pitting and Microbial Corrosion: Experimental and Theoretical Inspections, *Adv. Environ. Life Sci.*, 2022, 1–17.

2 M. M. kamel, S. M. Rashwan, M. A. A. Mahmoud, S. A. A. El-Mekawy, M. K. Awad and H. E. Ibrahim, Resorcinol Derivatives as an Environmentally Friendly Low Carbon Steel Inhibitor in HCl Medium, *ACS Omega*, 2022, **7**(21), 17609–17619.

3 (*a*) P. R. Roberge, *Handbook of Corrosion Engineering*. McGraw-Hill, New York, 2000; (*b*) M. B. Kermani, L. M. Smith, *CO_2 Corrosion Control in Oil and Gas Production: Design Considerations*, The Institute of Materials, European Federation of Corrosion Publications, London, 1997, 1.

4 N. Mouats, M. L. Belkadi, A. Bouyanzer, A. El Harfi, R. Saddik and A. Zarrouk, 2-(2,4,5-Trimethoxybenzylidene)hydrazine carbothioamide as a green corrosion inhibitor for Q235 steel in 1 M HCl: experimental and theoretical studies, *ACS Omega*, 2024, **9**, 27945–27962.

5 D. Lusk, M. Gupta, K. Boinapally and Y. Cao, Armoured against corrosion, *Hydrocarb. Eng.*, 2008, **13**, 115–118.

6 M. A. Migahed, M. M. Attya, M. Abd El-raouf, E. A. Khamis, T. A. Ali and A. M. Al-Sabagh, Corrosion inhibition of X-65 carbon steel in oil wells produced water under CO_2 environment, *Int. J. Electrochem. Sci.*, 2015, **10**, 1343–1360.

7 M. A. Migahed, A. A. Farag, S. M. Elsaed, R. Kamal and H. Abd El-Bary, Corrosion inhibition of steel pipeline in oil well formation water by a new family of nonionic surfactant, *Chem. Eng. Commun.*, 2012, **199**, 1335–1356.

8 R. A. El-Nagar, N. A. Khalil, Y. Atef, M. I. Nessim, A. Ghanem, *et al.*) Evaluation of ionic liquids based imidazolium salts as environmentally friendly corrosion inhibitors for carbon steel in HCl solutions, *Sci. Rep.*, 2024, **14**, 1889.

9 L. M. Rivera-Grau, M. Casales, I. Regla, D. M. Ortega-Toledo, J. G. Gonzalez-Rodriguez and L. Martinez Gomez, CO_2 corrosion inhibition by imidazoline derivatives based on coconut oil, *J. Electrochem. Sci.*, 2012, **7**, 13044–13057.

10 M. Heydari and M. Javidi, Corrosion inhibition and adsorption behavior of an amido-imidazoline derivative on API 5L X52 steel in CO2-saturated solution and synergistic effect of iodide ions, *Corros. Sci.*, 2012, **61**, 148–155.

11 P. C. Okafor, B. Liu, X. Liu and Y. G. Zheng, Inhibition of CO2 corrosion of N80 carbon steel by carboxylic quaternary imidazoline and halide ions additives, *J. Appl. Electrochem.*, 2009, **39**, 2535–2543.

12 J. Luo, A. Naik, A. Keshmiri, S. Khajuria and G. G. Gil, Understanding CO2 corrosion in multiphase flow: recent progress and future directions, *Corros. Sci.*, 2023, **224**, 111430.

13 M. Scendo and M. Hepel, Inhibiting properties of benzimidazole films for Cu (ii)/Cu (i) reduction in chloride media studied by RDE and EQCN techniques, *J. Electroanal. Chem.*, 2008, **613**, 35–50561.

14 J. G. Gonzalez-Rodriguez, T. Zeferino-Rodriguez, D. M. Ortega, S. Serna, B. Campillo, M. Casales, E. Valenzuela and J. Juarez-Islas, Effect of microstructure on the CO2 corrosion inhibition by carboxy amido imidazolines on a pipeline steel, *Int. J. Electrochem. Sci.*, 2007, **2**, 883–896.

15 A. A. El-Awady, B. A. Abd-El-Nabey and S. G. Aziz, Kineticthermodynamic and adsorption isotherms analyses for the inhibition of the acid corrosion of steel by cyclic and open-chain amines, *J. Electro. Chem. Sci.*, 1992, **139**, 2149–2154.

16 R. Padhi, B. Toth and M. R. Fitzsimmons, Molecular modeling of corrosion inhibitors: scope and limitations for predicting adsorption and free energies, *npj Mater. Degrad.*, 2024, **8**, 55.

17 A. Mishra, C. Verma, S. Chauhan, et al., Synthesis, Characterization, and Corrosion Inhibition Performance of 5-Aminopyrazole Carbonitriles Towards Mild Steel Acidic Corrosion, *J. Bio Tribo Corros.*, 2018, **4**, 53, DOI: 10.1007/s40735-018-0174-8.

18 F. Benhiba, A. Zarrouk, M. Zertoubi and A. Mohammed, Amino acid structure analog as a corrosion inhibitor of carbon steel in 0.5 M H2SO4: electrochemical, synergistic effect and theoretical studies, *Chem. Data Collect.*, 2020, **30**, 100586.

19 A. Alamri and I. Obot, Highly efficient corrosion inhibitor for C1020 carbon steel during acid cleaning in multistage flash (MSF) desalination plant, *Desalination*, 2019, **470**, 114100.

20 Z. Zhang, L. Zhang and C. Bao, Machine learning assisted equivalent circuit model and Bayesian assessment for corrosion behavior by EIS, *npj Mater. Degrad.*, 2024, **8**, 68.

21 A. Elaraby, S. El-samad, E. khamis and E. Zaki, Theoretical and electrochemical evaluation of tetra-cationic surfactant as corrosion inhibitor for carbon steel in 1 M HCl, *Sci. Rep.*, 2023, **13**, 942.

22 A. Berrissoul, A. Ouarhach, F. Benhiba, R. Abderrahmane, A. Guenbour, B. Dikici, F. Bentiss, A. Zarrouk and A. Dafali, Assessment of corrosion inhibition performance of origanum compactum extract for mild steel in 1 M HCl: weight loss, electrochemical, SEM/EDX, XPS, DFT and

molecular dynamic simulation, *Ind. Crops Prod.*, 2022, **187**, 115310.

23 M. E. Belghiti, Y. Karzazi, C. Jama and F. Bentiss, Anticorrosive properties of two 3,5-dissubstitud-4-amino-1,2,4-triazole derivatives on copper in hydrochloric acid environment: Ac impedance, thermodynamic and computational investigations, *Surf. Innovations*, 2020, **21**, 100692.

24 K. Seema, K. Kamlesh, H. Imad, S. Shriram, V. Aashish, K. Pankaj, *et al.*) Adenine-linked quinoline derivatives as efficient corrosion inhibitors for mild steel in 1 M HCl: experimental and computational studies, *J. Mol. Liq.*, 2024, **426**, 124932.

25 A. Ghani, H. Bahron, K. Harun and K. Kassim, Schiff bases derived from isatin as mild steel corrosion inhibitors in 1 M HCl, *Malays. J. Anal.Malays. J. Anal.*, 2014, **18**, 507–513.

26 A. Ashmawy, M. Mostafa, A.-B. Kamal. G. Ali and M. M. El-Gabya, *Study corrosion inhibitor for mild steel in 1M HCl by pyrazolone-sulfonamide hybrids: Synthesis, characterization evaluation as corrosion inhibitors*, 2023, DOI: 10.21203/rs.3.rs-3104311/v1.

27 W. Saad and A. El-Shamy, Unlocking the Potential of Cinnamaldehyde: A Comprehensive Study on Its Dual Role as an Effective Inhibitor against Corrosion and Microbial Corrosion of Mild Steel in Saline Environments, *J. Bio Tribo-Corrosion*, 2024, **10**, 14.

28 I. Annon, K. Jlood, M. Hanoon, F. Sayyid, W. Al-Azzawi and A. Al-Amiery, Corrosion Inhibition of Mild Steel in HCl Solution Using MPO: Experimental and Theoretical Insights, *J. Mater. Eng.*, 2024, **2**, 104–118, DOI: 10.61552/JME.2024.02.002.

29 I. Ahamad, R. Prasad and M. A. Quraishi, Inhibition of mild steel corrosion in acid solution by Pheniramine drug: Experimental and theoretical study, *Corros. Sci.*, 2010, **52**, 3033–3041.

30 M. A. Amin, M. A. Ahmed, H. A. Arida, F. Kandemirli, M. Saracoglu, T. Arslan and M. A. Basaran, Monitoring corrosion and corrosion control of iron in HCl by nonionic surfactants of the TRITON-X series-Part III. Immersion time effects and theoretical studies, *Corros. Sci.*, 2011, **53**, 1895–1909.

31 C. Cao, On electrochemical techniques for interface inhibitor research, *Corros. Sci.*, 1996, **38**, 2073–2082.

32 M. G. A. Saleh, S. M. Alshammari and S. A. Gheni, Hydrazine-carbothioamide Schiff base as an efficient corrosion inhibitor for carbon steel in HCl: experimental and DFT insights, *J. Electrochem. Sci. Eng.*, 2025, **15**(5), 2546.

33 N. A. Odewunmi, S. A. Umoren and Z. M. Gasem, Watermelonwaste products as green corrosion inhibitors for mild steel in HCl solution, *J. Environ. Chem. Eng.*, 2015, **3**, 286–296.

34 G. A. Zhang and Y. F. Cheng, Corrosion of X65 steel in CO2-saturated oilfield formation water in the absence and presence of acetic acid, *Corros. Sci.*, 2009, **51**, 1589–1595.

35 F. F. Eliyan, E. Mahdi and A. Alfanatazi, Electrochemical evaluation of the corrosion behaviour of API-X100 pipeline steel in aerated bicarbonate solutions, *Corros. Sci.*, 2012, **58**, 181–191.

36 S. A. Abd El-Maksoud, M. A. Migahed, M. M. Gouda and F. I. El-Dossoki, Novel gemini cationic thiazole-based surfactants as carbon steel corrosion inhibitors in 1 M HCl, *Sci. Rep.*, 2025, **15**, 17512.

37 S. B. Ghosh, S. Sarkar, S. Roy, S. Bandyopadhyay and S. Banerjee, Thermodynamic and kinetic investigation of a new benzotriazole-based compound as a corrosion inhibitor for mild steel in acidic medium: Experimental and theoretical insights, *J. Indian Chem. Soc.*, 2024, **102**, 101547.

38 M. A. Amin, M. A. Ahmed, H. A. Arida, F. Kandemirli, M. Saracoglu, T. Arslan and M. A. Basaran, Corrosion inhibition of mild steel in acidic medium using 4-aminantipyrine derivatives: Electrochemical, thermodynamic and quantum chemical studies, *Mater. Chem. Phys.*, 2008, **110**(2–3), 145–154.

39 M. A. Migahed, A. M. Al-Sabagh, M. R. Mishrif, H. M. Abd-El-Bary, Z. M. Mohamed and B. M. Hussein, Efficiency of nonionic surfactants based on oleic acid as corrosion inhibitors for Carbon Steel Pipelines in Deep Oil Formation Water Saturated with CO2 at 40 oC, *Res. J. Pharm. Biol. Chem. Sci.*, 2015, **6**, 726–744.

40 L. Chahir, M. El Faydy, L. Adlani, N. Abad, I. Warad, F. Benhiba, *et al.*) Explanation of the quinoxaline analog's adsorption and inhibition mechanism for carbon steel corrosion in 1 M HCl based on experiments and theoretical calculations, *Phys Chem. Res.*, 2024, **12**(4), 881–899.

41 M. Stern and A. L. Geary, Electrochemical Polarization I. A Theoretical Analysis of the Shape of Polarization Curves, *J. Electrochem. Soc.*, 1957, **104**, 56–63.

42 A. El-Sayed, H. S. Mohran and H. M. Abd El-Lateef, The inhibition effect of 2,4,6-tris (2- pyridyl)-1,3,5-triazine on corrosion of tin, indium and tin–indium alloys in hydrochloric acid solution, *Corros. Sci.*, 2010, **52**, 1976–1984.

43 N. A. Negm, M. A. Migahed, R. K. Farag, A. A. Fadda, M. K. Awad and M. M. Shaban, High-performance corrosion inhibition of novel tri cationic surfactants on carbon steel in formation water: Electrochemical and computational evaluations, *J. molliq.*, 2018, **262**, 363–375.

44 L. Chahir, M. El Faydy, L. Adlani, *et al.*) Inhibition performance of a novel quinoxaline derivative for carbon steel corrosion in 1 M HCl, *J. Electrochem. Sci. Eng.*, 2024, **14**(3), 275–296.

45 ISO 25178-2: (2012)-Geometrical Product Specifications (GPS), *Int. Org. Stand.*, **2012**.

46 A. Dehghani, G. Bahlakeh, B. Ramezanzadeh and M. Ramezanzadeh, Potential of Borage flower aqueous extract as an environmentally sustainable corrosion inhibitor for acid corrosion of mild steel: electrochemical and theoretical studies, *J. Mol. Liq.*, 2019, **277**, 895–911.

47 A. M. Al-Sabagh, N. M. El Basiony, S. A. Sadeek and M. A. Migahed, Scale and corrosion inhibition performance of the newly synthesized anionic surfactant in

desalination plants: experimental, and theoretical investigations, *Desalination*, 2018, **437**, 45–58.

48 A. G. Sayed, A. M. Ashmawy, W. E. Elgammal, S. M. Hassan and M. A. Deyab, Synthesis, description, and application of novel corrosion inhibitors for CS AISI1095 in 1.0 M HCl based on benzo[h]quinoline hydrazone derivatives, *Sci. Rep.*, 2023, **13**, 13761.

49 A. S. Fouda, M. A. Ismail, A. S. Abousalem and G. Y. Elewady, Experimental and theoretical studies on corrosion inhibition of 4-amidinophenyl-2, 20-bifuran and its analogues in acidic media, *RSC Adv.*, 2017, **7**, 46414–46430.

50 K. Efil and Y. Bekdemir, Theoretical study on corrosion inhibitory action of some aromatic imines with sulphanilic acid: a DFT study, *Canad. Chem. Trans.*, 2015, **3**, 85–93.

51 Z. Lakbaibi, M. Damej, A. Molhi, M. Benmessaoud, S. Tighadouini, A. Jaafar, B. Tariq, A. Ansari, A. Driouich and M. Tabyaoui, Evaluation of inhibitive corrosion potential of symmetrical hydrazine derivatives containing nitrophenyl moiety in 1M HCl for C38 steel: Experimental and Theoretical studies, *Heliyon*, 2022, **8**(3), e09087.

52 M. El Azzouzi, A. Aouniti, S. Tighadouin, H. Elmsellem, S. Radi, B. Hammouti, A. El Assyry, F. Bentiss and A. Zarrouk, Some hydrazine derivatives as corrosion inhibitors for mild steel in 1.0M HCl: weight loss, electrochemical, SEM and theoretical studies, *J. Mol. Liq.*, 2016, **221**, 633–641.

53 M. Galai, K. Dahmani, O. Kharbouch, M. Rbaa, N. Alzeqri, L. Guo, A. A. AlObaid, A. Hmada, N. Dkhireche, E. Ech-Chihbi and M. Ouakki, Surface analysis and interface properties of a newly synthesized quinoline-derivative corrosion inhibitor for mild steel in acid pickling bath: Mechanistic exploration through electrochemical, XPS, AFM, contact angle, SEM/EDS, and computational studies, *J. Phys. Chem. Solids*, 2024, **184**, 111681.

54 M. Abouchane, N. Dkhireche, M. Rbaa, F. Benhiba, M. Ouakki, M. Galai, B. Lakhrissi, A. Zarrouk and M. Ebn Touhami, Insight into the corrosion inhibition performance of two quinoline-3-carboxylate derivatives as highly efficient inhibitors for mild steel in acidic medium: Experimental and theoretical evaluations, *J. Mol. Liq.*, 2022, **360**, 119470.

55 A. Ech-chebab, M. Missioui, L. Guo, O. El Khouja, R. Lachhab, O. Kharbouch, M. Galai, M. Ouakki, A. Ejbouh, K. Dahmani and N. Dkhireche, Evaluation of quinoxaline-2(1H)-one derivatives as corrosion inhibitors for mild steel in 1.0 M acidic media: Electrochemistry, quantum calculations, dynamic simulations, and surface analysis, *Chem. Phys. Lett.*, 2022, **809**, 140156.

56 K. Dahmani, M. Galai, M. Rbaa, A. Ech-Chebab, N. Errahmany, L. Guo, A. A. AlObaid, A. Hmada, I. Warad, M. E. Touhami and M. Cherkaoui, Evaluating the efficacy of synthesized quinoline derivatives as corrosion inhibitors for mild steel in acidic environments: An analysis using electrochemical, computational, and surface techniques, *J. Mol. Struct.*, 2024, **1295**, 136514.

57 M. Oubaaqa, M. Ouakki, M. Rbaa, F. Benhiba, M. Galai, R. Idouhli, M. Maatallah, A. Jarid, I. Warad, B. Lakhrissi and A. Zarrouk, Experimental and theoretical investigation of corrosion inhibition effect of two 8-hydroxyquinoline carbonitrile derivatives on mild steel in 1 M HCl solution, *J. Phys. Chem. Solids*, 2022, **169**, 110866.

58 K. Dahmani, M. Galai, M. Ouakki, A. Elgendy, R. Ez-Zriouli, R. Lachhab, S. Briche and M. Cherkaoui, Corrosion inhibition of copper in sulfuric acid via environmentally friendly inhibitor (Myrtus Communis): Combining experimental and theoretical methods, *J. Mol. Liq.*, 2022, **347**, 117982.

59 A. Ech-chebab, K. Dahmani, R. Hsissou, O. El Khouja, D. K. Verma, E. Berdimurodov, Ş. Erdoğan, *et al.*, Anticorrosion properties of the epoxy polymer TGETBAU for mild steel in a solution of HCl (1.0 M): Experimental and computational approaches, *J. Mol. Struct.*, 2023, **1284**, 135441.